Modelling Cloud Droplet Formation

Rosalind West, August 2008

Transfer of status report

Supervised by Dr. Philip Stier, Dr. Don Grainger and Dr. Andy Jones

Contents

1 Introduction

The aim of this project is to improve the understanding of the indirect aerosol effects through a combination of computer modelling and satellite observations. The crucial link between aerosols and clouds is the ability of aerosols to act as centres of nucleation on which cloud droplets form. This microphysical process is impossible to explicitly include in a global climate model, and various parameterisations have been developed which attempt to enable this sub-grid-scale process to be represented in large-scale global models.

The aim for the first year is to implement one such parameterisation of cloud droplet formation into a general circulation model (GCM), specifically the UK Met Office Hadley Centre Global Environmental Model (HadGEM2). This GCM will then be used to investigate the complex interactions between aerosols, clouds and the climate at large.

These simulations will be compared with remote satellite observations of aerosol and cloud parameters from the A-train, a constellation of six co-located polar-orbiting satellites, and in situ measurement datasets. The constraints provided by these data will allow an improvement of the representation of the processes in the GCM, hopefully leading to a reduction in the current level of uncertainty in estimates of the indirect aerosol effects.

1.1 Aerosol radiative effects

Aerosols are liquid or solid particles suspended in the air. The effects of their presence in the atmosphere can be divided into direct and indirect effects, described in sections 1.1.1 and 1.1.2. While some aerosols are natural in origin, such as sea salt, organic matter and dust, the global mean aerosol burden of the atmosphere has increased considerably due to industrialisation [32]. Anthropogenic aerosols now play a significant role in the Earth's radiative balance.

The climate of the Earth is a complex system of myriad interacting processes and feedback loops. In order to discern and quantify the influence of a particular one of these processes on the radiative energy balance of the Earth it is necessary to define a standard property which may be compared between factors. Ramaswamy et al. (2001) define radiative forcing as 'the change in net (down minus up) irradiance (solar plus longwave in $\mathrm{W\,m^{-2}}$) at the tropopause after allowing for stratospheric temperatures to readjust to radiative equilibrium, but with surface and tropospheric temperatures and states held fixed at the unperturbed levels.' [40] In other words, the radiative forcing due to a particular process is the change in the Earth's energy balance that would occur if that factor alone were altered, and all other variables were held constant. A positive radiative forcing indicates an increase in the energy of the system leading to a warming effect, while negative indicates cooling. Radiative forcing is often used to assess the impact different factors have on climate, by comparing the total radiative forcing relative to the industrial revolution (starting in about 1750).

Figure 1 shows the global mean total radiative forcings over the period 1750 to 2005 for various climate forcing agents and mechanisms. Currently, the uncertainty in the radiative forcing due to the indirect aerosol effect is the greatest uncertainty amongst the known causes of radiative forcing. Reducing this level of uncertainty will reduce the overall uncertainty in radiative forcing of the climate and provide tighter constraints for climate modelling and prediction.

1.1.1 Direct effect

The direct effect of aerosol particles on the radiative balance of the Earth involves a combination of scattering and absorption of radiation by the aerosol particles themselves. As shown in figure 1, this effect is estimated to contribute a net radiative forcing of $-0.5\,\mathrm{W\,m^{-2}}$ [±0.40] [12], a net cooling

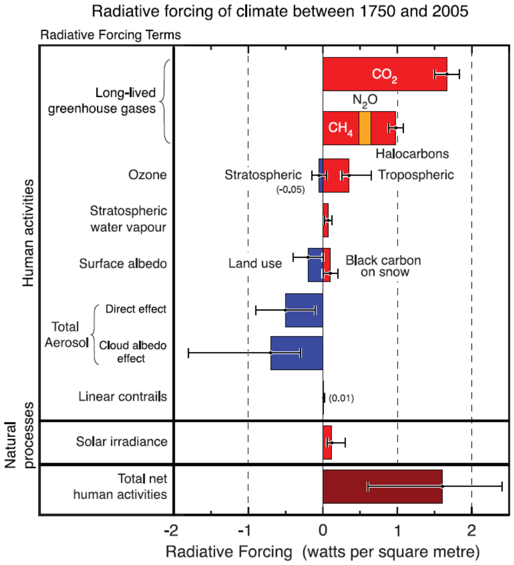

Fig. 1: Summary of the principal components of the radiative forcing of climate change. The values represent the forcings in 2005 relative to 1750. The current range of uncertainty in the radiative forcing of each component is shown by a black error bar. From IPCC (2007) [12]

effect. The 'semi-direct effect' is the mechanism by which absorption of shortwave (solar) radiation by tropospheric aerosols leads to heating of the troposphere that in turn changes the relative humidity and the stability of the troposphere [12]. This could hinder cloud formation, and/or cause existing cloud droplets to evaporate [32]. The semi-direct effect is not strictly classed as a radiative forcing by the IPCC [12], due to modifications to the hydrological cycle, so it does not feature in figure 1.

1.1.2 Indirect effects

Aerosols also affect the radiative balance due to their interactions with clouds. The presence, lifetime, abundance and properties of clouds may all be modified by the aerosols present in the surrounding environment. Cloud formation itself is dependent on the presence of aerosols to act as centres of nucleation for droplet formation (section 2.1.1).

The indirect effects are conventionally split into two main effects, and a number of other less well understood processes. The first of these is the cloud albedo effect, also known as 'the Twomey effect' or simply 'the first indirect effect'. In a cloud of constant liquid water content, a greater number concentration of aerosol particles leads to a greater number of smaller cloud droplets which leads to an enhanced reflection of solar radiation (due to increased surface area of the droplets) and hence an increased cloud albedo [47, 48, 51].

The second indirect effect relates to the lifetime of clouds. An increase in the number concentration of aerosol particles leads to a greater number of smaller cloud droplets and hence reduces the precipitation efficiency of the cloud as smaller droplets take longer to grow to a size necessary to precipitate out. This increases the lifetime of the cloud, and hence also its reflectivity over time [6].

The indirect aerosol effects are difficult to quantify, because the physical processes are difficult to parameterise in GCMs and satellite retrievals of aerosol–cloud interactions are also challenging [39]. Nevertheless, as shown in figure 1, the IPCC estimate a net radiative forcing of $-0.70\,\mathrm{W\,m^{-2}}$ $[-1.1, +0.4]$ for the cloud albedo effect.

2 Aerosol activation

2.1 Cloud formation

The formation of clouds in the atmosphere is possible due to a combination of thermodynamic and microphysical processes. For a cloud to form, it is necessary for a large volume of moist air to be cooled below its dew point. The dew point temperature, T_d, is defined as the temperature to which moist air must be cooled, at constant pressure and mixing ratio, for it to reach saturation with respect to water. (Where mixing ratio, w, is the ratio of mass of water vapour, M_v to mass of dry air, M_d, per unit volume of moist air, $w = M_v/M_d = \rho_v/\rho_d$.) A parcel of air which is saturated with respect to water defines the concept of relative humidity, since relative humidity, f, is defined as the mixing ratio of a parcel at a particular temperature and pressure, compared to its saturation mixing ratio value at the same temperature and pressure,

$$f = \frac{w}{w_s(p,T)} \approx \frac{e}{e_s}, \tag{1}$$

where e is the vapour pressure of water in the parcel, and e_s is the saturated (equilibrium) vapour pressure of water over a plane surface of water at the temperature of the parcel. A parcel is described as supersaturated when $e > e_s$. The temperature dependence of e_s is defined by the Clausius–Clapeyron equation:

$$\frac{de_s}{dT} = \frac{L}{T(v_v - v_l)} \tag{2}$$

where L is the latent heat of vaporisation, and v_v and v_l are the specific volumes of water vapour and liquid water. In ordinary atmospheric conditions, $v_v \gg v_l$ and water behaves as an ideal gas, ($e = \rho_v R_v T$, where R_v is the ideal gas constant), so equation 2 reduces to

$$\frac{de_s}{dT} = \frac{L}{Tv_v} = \frac{Le_s}{R_v T^2}. \tag{3}$$

The temperature dependence of L makes an analytic expression for $e_s(T)$ impossible, but various approximations can be made depending on the applicable temperature range [15, 41].

In the atmosphere, the most prevalent mechanism for a parcel of moist air to be cooled below T_d is via the approximately adiabatic expansion of ascending air, although it can be caused by radiative cooling or due to the convergence of air parcels with different temperatures and moisture contents. In an ascending parcel, the updraught velocity affects the rate of cooling and hence the amount of condensation which forms. However, the condensation of water into individual cloud droplets is governed by complex processes on a far smaller scale [41].

2.1.1 Cloud microphysics

In supersaturated air, cloud droplets may form by either of two microphysical processes. Homogeneous nucleation is the nucleation of water vapour onto embryonic droplets themselves consisting only of water [42]. This requires the initial formation of tiny embryonic droplets (clusters of water molecules) with a very tightly curved surface. The effect of this curvature is that the saturated vapour pressure over the embryo is much higher than that over a plane surface of water, as described by the Kelvin effect (section 2.2.1). As a result, the saturation ratio (actual vapour pressure divided by saturated vapour pressure over a plane surface) required for droplets to form on these clusters is predicted to be of the order 3.5 to 8. Experimentally, relative humidities of over 800% have been reached, in air free of all impurities and ions, before cloud droplets will form spontaneously in an expansion chamber [37].

The abundance of aerosols in the atmosphere provides an alternative mechanism for droplet formation at far lower supersaturations. As a result, levels of supersaturation required for homogeneous nucleation are never reached [7]. Heterogeneous nucleation, the condensation of water on a foreign substance or surface, is favourable because of the reduction in saturation vapour pressure over the droplet either due to the presence of a solute (discussed in section 2.2.2) or due to the opposition of the Kelvin effect provided by the presence of an insoluble core which increases the radius of curvature of the droplet.

2.2 Köhler theory

2.2.1 Curvature effect

For droplets to grow, the rate of condensation of water onto the droplet must exceed the evaporation from the surface. First, consider the process of homogeneous nucleation on a spherical droplet of water. The vapour pressure over a curved surface as a function of radius, $e_s(r)$ will be discussed with respect to the vapour pressure over a plane surface, $e_s(\infty)$. Consider the change in Gibbs free energy due to the formation of a single droplet of radius r containing n molecules of water

$$\Delta G = G_{\text{droplet}} - G_{\text{pure vapour}}. \tag{4}$$

Let the total initial number of molecules be N_T, and the number of molecules remaining in the vapour state after the droplet forms be $N_T - n = N_v$. Let g_v and g_l be the Gibbs free energies of a molecule in the vapour or liquid state, respectively. Then

$$\Delta G = N_v g_v + n g_l + 4\pi r^2 \sigma - N_T g_v, \tag{5}$$

where $4\pi r^2 \sigma$ represents the work required to create the spherical surface between the liquid and vapour, and σ is the surface tension. This may be rewritten as

$$\Delta G = n(g_l - g_v) + 4\pi r^2 \sigma. \tag{6}$$

The number of molecules in the droplet is $n = \frac{4}{3}\pi r^3 / v_l$, where v_l is the volume occupied by a molecule in the liquid phase. This can be included to give

$$\Delta G = \frac{4\pi r^3}{3v_l}(g_l - g_v) + 4\pi r^2 \sigma. \tag{7}$$

The Gibbs free energy G is defined as

$$G = U + pV + TS \tag{8}$$

and chemical potential, μ_i of a species i is defined by

$$\mu_i = \left(\frac{\partial U}{\partial n_i}\right)_{S,V,n_j} \tag{9}$$

where n_i is the number of moles of species i. By using the differential form of equation 8 and combining with the differential form of the thermodynamic relation for the internal energy of a system of variable composition, incorporating the chemical potential from equation 9 we obtain

$$dG = -SdT + Vdp + \sum_{i=1}^{k} \mu_i dn_i. \tag{10}$$

At constant temperature, and fixed number of molecules, this reduces to $dg = vdp$ or $dg = (v_l - v_v)dp$. In the relevant limit $v_v \gg v_l$, so neglecting v_l relative to v_v gives $dg = -v_v dp$. Assume the vapour to be an ideal gas so $v_v = kT/p$. Integrating gives

$$g_l - g_v = -kT \int_{e_s(\infty)}^{e_s(r)} \frac{dp}{p} = -kT \ln\left(\frac{e_s(r)}{e_s(\infty)}\right). \tag{11}$$

Defining the saturation ratio, $s = e_s(r)/e_s(\infty)$ and substituting equation 11 into equation 7 gives the following expression for the Gibbs free energy associated with homogeneous nucleation of a spherical droplet

$$\Delta G = -\frac{4\pi r^3}{3v_l} kT \ln s + 4\pi r^2 \sigma. \tag{12}$$

The sign of the first term on the right hand side is defined by the saturation ratio, and this has a strong effect on the behaviour of ΔG as a function of r. In subsaturated conditions, $e_s(r) < e_s(\infty)$ so $\ln s$ is negative, and hence ΔG is always positive and increases with increasing r. This inhibits droplet formation under subsaturated conditions. In supersaturated conditions, $e_s(r) > e_s(\infty)$ so $\ln s$ is positive. In this case, ΔG can be positive or negative, depending on the value of r. Initially, ΔG increases with increasing r, inhibiting the growth of very small particles in supersaturated conditions. ΔG reaches a maximum at $r = r^*$ and then decreases with further increase in r, allowing a droplet to continue growing spontaneously through condensation from the vapour phase, since further growth causes a further drop in ΔG. The maximum is a metastable equilibrium, and its location can be found by setting $\partial \Delta G/\partial r = 0$ in equation 12 to obtain

$$r^* = \frac{2\sigma v_l}{kT \ln s}. \tag{13}$$

This equation relates the equilibrium radius of a droplet of pure substance (in our case, water) to the physical properties of that substance, σ and v_l, and the saturation ratio over the droplet in its environment. It can be re-expressed in terms of molar units as the more familiar Kelvin equation

$$\frac{e_s(r)}{e_s(\infty)} = \exp\left(\frac{2\sigma M_w}{\rho_w R T r}\right) = \exp\left(\frac{A}{r}\right), \tag{14}$$

where

$$A = \frac{2\sigma M_w}{\rho_w R T}. \tag{15}$$

It is apparent from the Kelvin equation that the vapour pressure over a curved surface of a substance is always greater than the vapour pressure over a plane surface of the same substance [42, 50]. Ultimately, because of this Kelvin effect, the larger a droplet, the faster it will grow, as described in section 2.2.3.

2.2.2 Solute effect

Many aerosols are soluble in water, and form a droplet of aqueous solution as water condenses on to them. In terms of droplet growth, this solubility is fortunate because the vapour pressure over a solution is lowered by the presence of the solute and hence growth is energetically favourable. The fractional reduction in vapour pressure due to the presence of a solute is given by Raoult's law, which states that the vapour pressure of an ideal solution is dependent on the vapour pressure of each chemical component and the mole fraction of the component present in the solution, so

$$\frac{e'}{e_s(\infty)} = \frac{n_w}{n_w + n_s}, \tag{16}$$

where e' is the vapour pressure of a solution consisting of n_w moles of water and n_s moles of dissolved solute. For a dilute solution, where $n_s \ll n_w$, we may expand binomially to give

$$\frac{e'}{e_s(\infty)} \approx 1 - \frac{n_s}{n_w}. \tag{17}$$

Number of moles of solute, $n_s = \nu m_s/M_s$ where m_s is mass of solute, M_s is molecular mass of solute and ν represents the degree of ionic dissociation of the solute and moles of water is given by $n_w = m_w/M_w$. Mass of solute present, $m_s = \frac{4}{3}\pi r_s^3 \rho_s$ where r_s is the radius of the dry solute particle before condensation of water, and ρ_s is the density of the solute. Mass of water in the droplet $m_w = \bar{v}_w \rho_w$, where $\bar{v}_w$ is the partial volume of water in the solution. In fact, since we are considering dilute solutions, we will approximate $\bar{v}_w \approx v = \frac{4}{3}\pi r^3$, where r is the droplet radius. Thus we may rewrite

$$\frac{e'}{e_s(\infty)} \approx 1 - \frac{\nu M_w r_s^3 \rho_s}{M_s r^3 \rho_w} = 1 - B\frac{r_s^3}{r^3}, \tag{18}$$

where

$$B = \frac{\nu M_w \rho_s}{M_s \rho_w} \tag{19}$$

is termed the Köhler hygroscopicity coefficient [50].

2.2.3 Köhler curves

For a droplet of solution these two effects are combined such that

$$\frac{e_s'(r)}{e_s(\infty)} = \left(1 - B\frac{r_s^3}{r^3}\right)\exp\left(\frac{A}{r}\right). \tag{20}$$

Expanding the exponential as a power series and defining supersaturation as $S = s - 1$, where $s = e_s'(r)/e_s(\infty)$ is the saturation ratio, gives a simplified version of the Köhler equation [41, 37, 42]:

$$S = \frac{e_s'(r)}{e_s(\infty)} - 1 \approx \frac{A}{r} - B\frac{r_s^3}{r^3}. \tag{21}$$

Each individual Köhler curve is specific to the amount and composition of solute in the growing droplet (i.e. the dry radius, r_s) and composition of the initial aerosol particle. In figure 2, supersaturation over the droplet is plotted as a function of the increasing wet radius of the aqueous droplet, r, formed as the dry aerosol particle dissolves in the accumulating water.

At small radii the solute term dominates. As the droplet grows, the solution becomes more dilute and the Kelvin term dominates, which gives rise to the distinctive shape of the Köhler curve shown in figure 2(a) and also illustrated in figure 3. Differentiating supersaturation with respect to radius provides the location of the maximum of this curve at a critical supersaturation of

$$S_c = \frac{2}{\sqrt{B}}\left(\frac{A}{3r_s}\right)^{3/2}, \tag{22}$$

and critical radius of

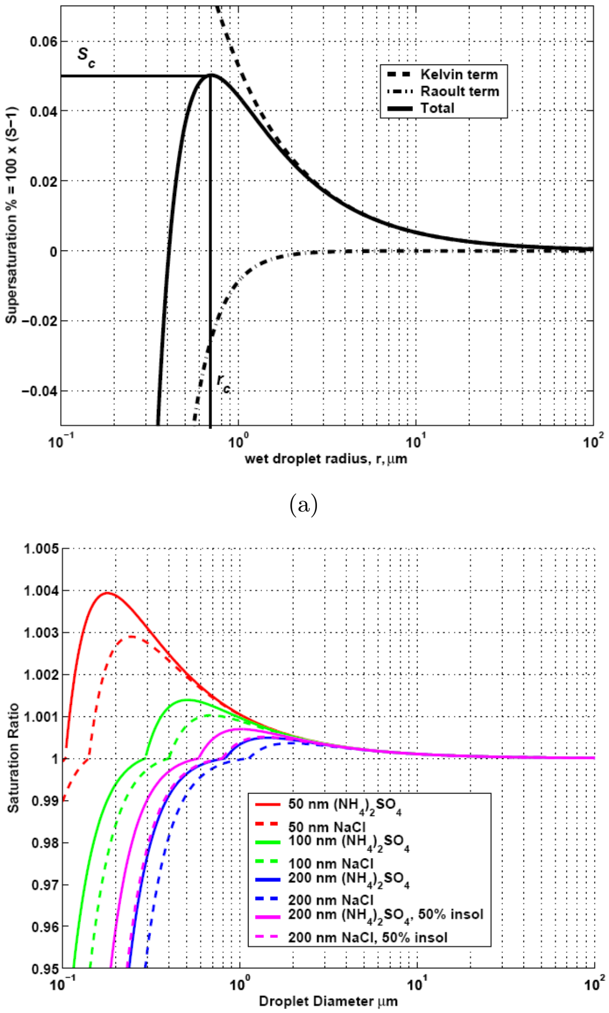

(a)

(b)

Fig. 2: Competition between the curvature (Kelvin) and solute (Raoult) terms is shown in (a). The location of S_c and r_c are shown at the maximum of the curve. In (b) the dependence of activation on dry size is highlighted. Köhler (activation) curves are shown for a range of dry diameter of salt particles ($(NH_4)_2SO_4$ with solid line, NaCl with dashed line). Red, green and blue lines indicate different dry diameters. Magenta lines are for a 200nm particle containing 50% by mass insoluble core. Both from McFiggans, 2006 [34].

$$r_c = \sqrt{\frac{3Br_s^3}{A}}. \tag{23}$$

Beneath these critical values of supersaturation and radius a droplet will be in stable equilibrium with the surroundings. If the relative humidity increases slightly, the droplet will grow slightly along the curve. Should the relative humidity drop, the droplet will evaporate slightly until the vapour pressure over the droplet surface is in equilibrium with the ambient vapour pressure. If the relative humidity is increased to the critical supersaturation, the droplet will grow to the critical radius. Up to this critical point, an increase in droplet radius is dependent on an increases in ambient relative

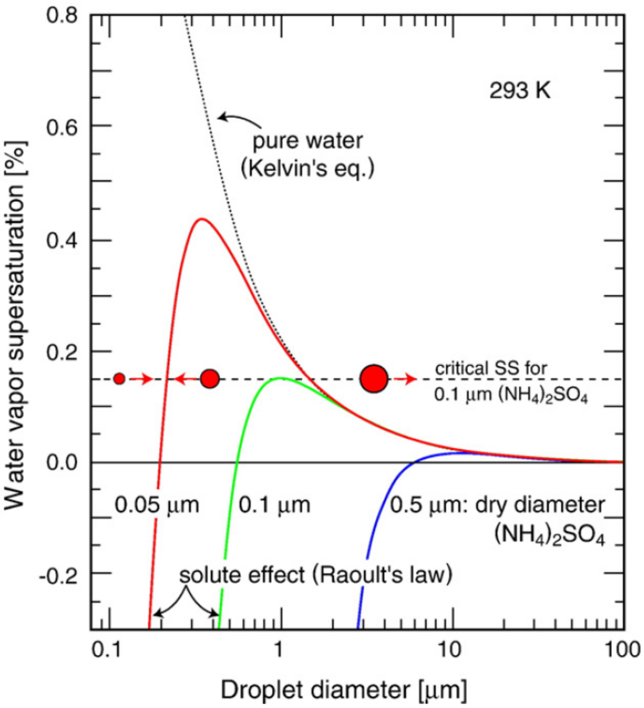

Fig. 3: Köhler curves at 293K for pure water (dotted line) and a range of dry diameter (denoted by colour) of $(NH_4)_2SO_4$ particles (solid lines). Dashed line indicates an ambient water vapour supersaturation, $S = 0.15\%$ which exceeds the critical supersaturation for $(NH_4)_2SO_4$ particles with dry diameter $\geq 0.1\,\mu$m, so these aerosols will activate and grow into cloud droplets. Smaller particles remain as unactivated haze particles. Indicated drops (corresponding, for example, to a dry diameter of $0.05\,\mu$m) show how these haze particles return to their equilibrium curve through condensation or evaporation. From Andreae and Rosenfeld (2008) [7] after Seinfeld and Pandis (1998) [42].

humidity. However, the significance of this critical point is that beyond it the Kelvin term dominates to such an extent that the vapour pressure over the droplet falls as the radius increases. Since the supersaturation over the droplet is less than the ambient supersaturation, water will continue to condense onto the droplet and hence the droplet will continue to grow in a runaway process, given a sufficient source of water vapour [29, 37, 42, 50]. These properties of the Köhler curve are illustrated in figure 3.

2.3 Activation

A droplet which has grown to such a size that it exceeds its critical radius is said to be activated. Particles that can activate at a given supersaturation are defined as cloud condensation nuclei (CCN) for this supersaturation. Since activation is dependent upon the S_c of each particle being equalled or exceeded by the ambient supersaturation, the number of particles from a given aerosol population that can act as CCN is a function of the supersaturation.

Of course, such a droplet can only continue to grow beyond activation while there is still water vapour available to condense onto it. In the atmosphere there will usually be many particles competing for the available water vapour, and this provides a natural limit to the droplets' growth. The maximum supersaturation in a rising parcel of air occurs when the water vapour availability due to the parcel cooling as it rises balances the depletion rate of water vapour by those droplets that have already activated [37]. This relationship plays a fundamental role in modelling droplet formation.

3 Aerosol populations

3.1 Aerosol size distributions

The activation of dry aerosol particles to cloud droplets is strongly dependent on the dry radius of the aerosol particle, as shown in figure 2(b) above. Aerosol particles cover a vast size range, from a few nanometres to tens of microns for large particles from combustion, sea salt or dust [41]. In the troposphere, the density of aerosol particles varies from about $1\,\mathrm{cm}^{-3}$ in a clean marine environment such as the southern oceans to over $10,000\,\mathrm{cm}^{-3}$ in heavily polluted continental urban regions such as Guangzhou and Beijing [7]. Of course, it would be computationally extortionate to attempt to track each particle individually, so instead various attempts have been made to mathematically describe aerosols with a number–size distribution.

In a sectional representation, particle size range is divided into discrete intervals, with the number concentration N_i, in each interval normalised by the width of the interval, Δr, such that the value of the aerosol distribution for a given interval, i, is $n_i = N_i/\Delta r$. In this case the area beneath the curve is proportional to the number concentration. As the size intervals tend to the infinitesimal limit, $\Delta r \to 0$, rewrite Δr as dr and define the size distribution $n_N(r)dr$ as the number of particles per unit volume in the size interval r to $r + dr$. Hence, the total number concentration of particles is

$$N = \int_0^\infty n_N(r)dr, \tag{24}$$

assuming the number distribution is a continuous function of radius (valid beyond a certain number of particles [42]). Equivalently,

$$n_N(r) = \frac{dN}{dr}. \tag{25}$$

Since the size distribution generally covers so many orders of magnitude, a logarithmic scale is often convenient, where the distribution function $n_N^e d(\ln r)$ is the number concentrations of particles with radius in the interval $d(\ln r)$ such that the cumulative distribution and total number concentration are

$$n_N^e(r) = \frac{dN(r)}{d(\ln r)} \quad \text{and} \quad N = \int_{-\infty}^{\infty} n_N^e(\ln r)d\ln r. \tag{26}$$

These distributions describe how the number concentration of particles varies as a function of radius (or log radius). In the early stages of aerosol science, aerosol number size distributions were often plotted as $\frac{dN(r)}{d(\ln r)}$ against $\ln r$. As shown in figure 4(a), this results in a near straight line, and led to the representation of size distributions by a power law or Junge distribution [26, 10], where

$$\frac{dN(r)}{d(\ln r)} = Cr^{-\alpha} \tag{27}$$

and the slope of the line on a log–log plot is given by $-\alpha$. However, assuming the initial dry aerosol particles are spherical, size distribution in terms of number is trivially transformable to a corresponding size distribution in terms of surface area or volume. Once this transformation is

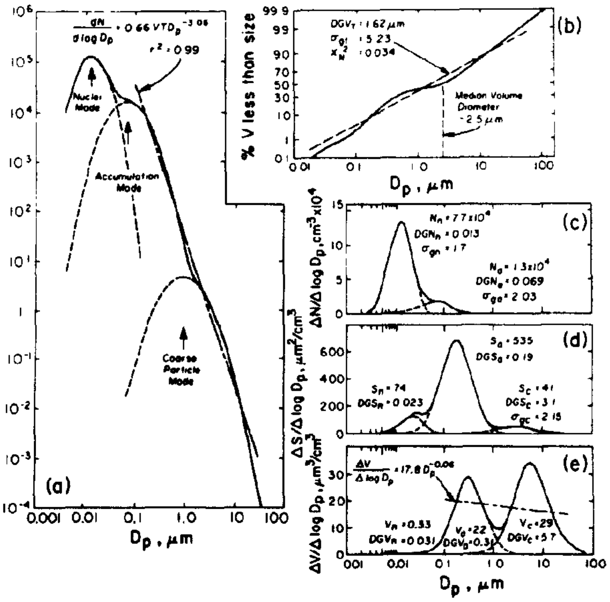

Fig. 4: Average urban aerosol plotted in five different ways. In (a), a power law function has been fitted to the number distribution over the size range $0.0 < D < 32.0\,\mu$m. In (b), a log-normal distribution has been fitted to the range $0.1 < D < 32.0\,\mu$m. It is evident that the modal nature of the aerosol is shown best by the plots of (c), (d) and (e). From Whitby (1978) [52].

performed, and the aerosol distribution replotted in terms of surface area or volume, as shown in figure 4(b), (c) and (d), it becomes apparent that those minor deviations from the straight line of the power law are actually significant modes. Amongst others, Whitby proposed that these modes can be represented by a sum of three log-normal distributions [52].

In a log-normal distribution [5], $f(x)$, the logarithm of x is normally distributed, such that if $f(x)$ is plotted against $\ln x$, the familiar bell-shaped curve is retrieved. The distribution can be defined simply by the geometric mean value of x, and the geometric standard deviation of the distribution, σ_g. Atmospheric aerosol size distributions are often described by the sum of I log-normal modes

$$\frac{dN(r)}{d(\ln r)} = \sum_{i=1}^{I} \frac{N_i}{\sqrt{2\pi}\ln\sigma_i} \exp\left\{ -\frac{\ln^2(a/a_{m,i})}{2\ln^2\sigma_i} \right\} \tag{28}$$

where N_i, $a_{m,i}$ and σ_i are the total number concentration, geometric mean dry radius and geometric standard deviation of aerosol mode i respectively [49, 2]. A trivial transformation converts this log-normal number distribution to a surface or volume distribution. One of the great advantages of this function is that such moment distributions (i.e. related by a power law) of the original log-normal distribution are also log-normal, and share the same geometric standard deviation [18, 42, 21].

3.2 Atmospheric aerosols

Aerosols are found in the atmosphere due to a variety of natural processes such as the eruption of volcanoes, sea spray and dust lifted by the wind. The combustion of fuel causes a significant amount of anthropogenic aerosol to be added to this concoction. Primary aerosols are those which are emitted directly as particulates and through the disintegration and dispersion of solids and liquids,

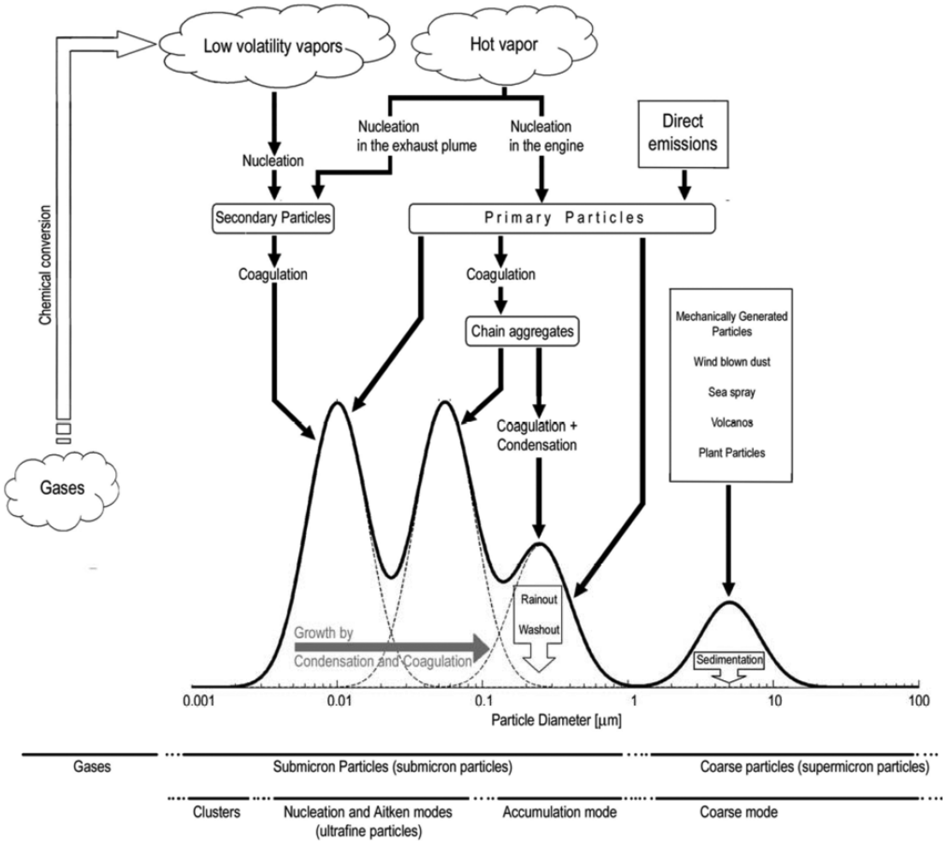

Fig. 5: Idealised schematic of an atmospheric aerosol number–size distribution. Principle modes, sources, and particle formation and removal mechanisms are indicated. From Hussein (2005) [22] after Whitby (1978) [52].

whereas secondary aerosols are formed through the condensation of low-volatility compounds [7]. Once airborne, aerosol particles may undergo a series of changes as their size and composition are modified due to their interactions with the surrounding environment and one-another. During their short atmospheric lifetime of a few days to a few weeks, possible interactions include: condensation of gases onto existing particles, evaporation, chemical reactions, coagulation with other particles or activation to become cloud droplets. As a result of these processes, most aerosols are composites of various chemical components, both soluble and insoluble. Aerosols are finally removed from the atmosphere due to their incorporation into cloud droplets and subsequent precipitation (wet deposition), or sedimentation (dry deposition) [42].

Aerosols are traditionally categorised into fine particles (diameter, $D < 2.5\,\mu\mathrm{m}$) and coarse particles ($D > 2.5\,\mu\mathrm{m}$). The fine particles are further split into the Aitken (or nucleation) mode ($0.005 < D < 0.1\,\mu\mathrm{m}$) and the accumulation mode ($0.1 < D < 2.5\,\mu\mathrm{m}$). While the Aitken mode accounts for the largest number of particles, it only accounts for a few percent of the mass. The accumulation mode usually contains the greatest fraction of surface area, and a significant proportion of the mass of the distribution. The bulk of the mass is contained within the coarse mode. In figure 5 the Aitken mode is split into a further two modes–confusingly also termed nucleation and Aitken–but since the fate of the tiny and numerous nucleation particles is predominantly to 'nucleate' (coalesce) to form bigger particles and hence transfer to the Aitken mode, three modes is a more

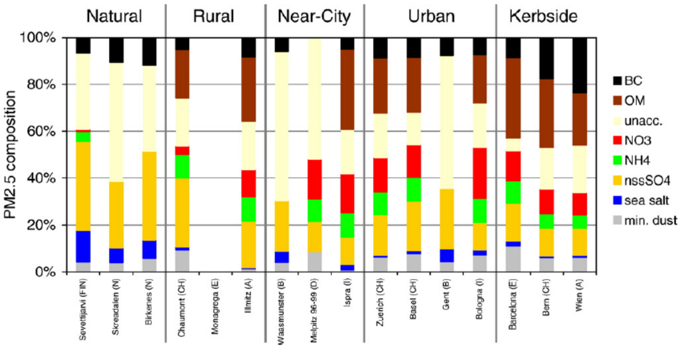

Fig. 6: Aerosol composition (PM2.5 i.e. fine particles) from a wide range of sampling environments ("natural" to curbside) in Europe. From Andreae and Rosenfeld (2008) [7] after Putaud et al. (2004) [38].

typical representation. Indeed the paper that this diagram originates from does not make this distinction [52].

Since the geographical variation in aerosol sources is so great, and the lifetime of aerosols in the atmosphere relatively short, the concentration and composition of aerosols in the troposphere varies considerably depending on location. Figure 6 shows typical composition in various continental regions of Europe.

In terms of modelling, a detailed emissions dataset is a necessary but insufficient prerequisite for useful incorporation of the aerosol activation process into a global model. What is needed additionally is knowledge of the 4D (space and time) evolution of the distribution of CCN, in the form of a comprehensive, interactive aerosol chemistry transport model [7].

3.2.1 Aerosols as CCN

Various properties of an aerosol particle affect its ability to act as a cloud condensation nucleus (CCN), the most important being its size and soluble mass fraction (see section 2.2). Further chemical effects can also modify the propensity of an aerosol—particularly an organic aerosol—to act as a CCN. Ambient soluble gases, especially HNO_3, NH_3 and HCl can dissolve in nascent droplets, increasing their soluble mass fraction, and hence the rate of droplet growth [30, 19, 36]. The presence of slightly soluble substances, especially organic compounds, can also increase the soluble mass fraction of the aerosol as relative humidity reaches 100% [17]. In the right conditions, even insoluble wettable aerosols can act as CCN due to the reduction in droplet radius and dominance of the Kelvin term over the solute term at larger radius [1]. Organic substances can reduce the surface tension in a droplet, aiding droplet growth [43]. However, organic constituents can also lead to the formation of a hydrophobic surface film, repelling water vapour and inhibiting activation or further growth [27]. A review of the nature and sources of cloud-active aerosols is given by Andreae and Rosenfeld (2008) [7].

Observations and modelling studies indicate that after some time in the atmosphere, most aerosols are internally mixed conglomerate particles, although the composition is not necessarily uniform across particular size classes [34]. Currently however, in terms of modelling, variation in composition across a mode is difficult to represent. Instead, most models either assume a sum of uniform internally mixed modes, or use a sectional representation of the size distribution, where the composition can be defined separately for each section.

4 Aerosol–cloud interactions in a GCM

4.1 Empirical relationships

The first attempts to represent and quantify aerosol–cloud interactions in a GCM relied on an empirical relationship between cloud droplet number concentration (CDNC) and total aerosol mass [8, 25] or total aerosol number [16]. Both Boucher and Lohmann [8], and Jones et al. [25], relate the sulphate aerosol mass concentration to CDNC using different empirically-derived relationships. However, there is a large amount of uncertainty inherent in both stages of this method: uncertainty in relating aerosol and CCN number concentration to sulphate mass concentration and uncertainty in relating CDNC concentration to CCN concentration (due to the complexities of aerosol activation as presented here). The complexity of aerosol–cloud interactions is such that a simple correlation based on a single aerosol property is bound to be a gross over-simplification. This is emphasised by a comparison of four different empirical relationships, including the two described, by Kiehl et al. (2000) [28], yielding a very broad estimated range of the globally averaged radiative forcing due to the indirect aerosol effect from $-1.78\,\mathrm{W\,m^{-2}}$ to $-0.40\,\mathrm{W\,m^{-2}}$.

4.2 Parameterising aerosol activation

There are two distinct stages to modelling cloud droplet formation on aerosol in known atmospheric conditions. First, the aerosol distribution itself must be well-defined, in terms of its chemical composition and size distribution. (For log-normal number-size distributions, this requires knowledge of the geometric mean radius and geometric standard deviation of each mode, the chemical composition of the uniform internal mixture of each mode, and the number concentration of particles in each mode. Knowledge of the chemical composition of particles in each mode must include as a minimum the soluble mass fraction, degree of ionisation of soluble components, and the molecular mass of both soluble and insoluble components, but can also include information relating to the additional chemical effects described above (section 3.2.1).)

Secondly, each size and composition of initial dry aerosol particle has its own Köhler curve, and hence its own particular critical supersaturation level required for it to activate into a cloud droplet. Equation 22 is used to calculate the critical supersaturation, S_c, for every single dry aerosol particle present, such that the size distribution, $N(r)$, can be re-expressed in supersaturation space giving the potential number of droplets that could form as a function of supersaturation. This distribution, $N(S)$, is called the CCN spectrum. (A modified version of Köhler theory can be used to include the effects of surfactant and slightly soluble species [43, 35]. See section 5.2.)

The number of droplets that actually form depends on the maximum level of supersaturation reached in the surrounding air parcel, S_{max}, determined by the atmospheric conditions and aerosol distribution. The CCN spectrum, $N(S)$, is integrated beneath S_{max} to give the total number of droplets formed, N_d.

4.3 Calculating maximum supersaturation

As an air parcel rises adiabatically it expands and cools. As it cools, the equilibrium vapour pressure of water vapour decreases (the temperature dependence of vapour pressure is given by the Clausius–Clapeyron equation (equation 2)), and since the total water content of the parcel stays constant, the supersaturation increases (see equation 21). The faster the parcel rises, the faster it cools and the greater the change in supersaturation with time. In terms of aerosol activation this is good news: greater updraught velocity and hence higher supersaturation in the parcel means a greater tendency for water vapour to condense onto the CCN and form cloud droplets. However, once activated, water vapour will continue to condense on the cloud droplets as they continue to grow, decreasing the supersaturation. The dry aerosol particles must then compete with already-activated droplets for the available water vapour. The balance between these two effects on the rate of change of supersaturation with time can be expressed as

$$\frac{dS}{dt} = \alpha V - \gamma \frac{dW}{dt}, \tag{29}$$

where V is the vertical updraught velocity of the parcel and $\frac{dW}{dt}$ is the rate of condensation of liquid water onto droplets, and α and γ are size-invariant coefficients [37, 42]:

$$\alpha = \frac{gM_wL}{c_pRT^2} - \frac{gM_a}{RT}, \quad \gamma = \frac{pM_a}{e_s(\infty)M_w} - \frac{M_wL^2}{c_pRT^2}. \tag{30}$$

The maximum supersaturation S_{max} can be found when $\frac{dS}{dt} = 0$. The water condensation rate during activation is given by

$$\frac{dW}{dt} = 4\pi\rho_w \int_0^S r^2 \frac{dr}{dt} n(S')dS', \tag{31}$$

where $n(S')dS'$ is the number concentration of particles that activate between supersaturation $S'$and $S' + dS'$ and ρ_w is water density. Substitute the growth rate of a droplet, $\frac{dr}{dt}$ where r is the radius of the droplet (not to be confused with the dry radius of the original aerosol particle, r_s) [37]

$$\frac{dr}{dt} = \frac{G}{r}\left(S - \frac{A}{r} + \frac{Br_s^3}{r^3}\right) \tag{32}$$

where the growth coefficient, G, is size-dependent due to gas kinetic effects and defined as

$$G = \frac{1}{\dfrac{\rho_w RT}{e_s(\infty)D_vM_w} - \dfrac{L\rho_w}{K_aT}\left(\dfrac{LM_w}{RT} - 1\right)}, \tag{33}$$

where K_a is the thermal conductivity of air and D_v is the water vapour diffusivity. Integrating equation 32 from the time, τ when the parcel supersaturation equals the supersaturation required to activate a particle with the count median radius, to the time when maximum supersaturation is reached, t_{max}, gives the radius of the droplet at the time of S_{max}

$$r^2(t) = r^2(\tau) + 2G\int_\tau^{t_{max}} S(t)dt. \tag{34}$$

Substituting into equation 31 gives the water condensation rate as

$$\frac{dW}{dt} = 4\pi\rho_w GS \int \left(r^2(\tau) + 2G\int_\tau^{t_{max}} S(t)dt\right)^{1/2} n(S')dS'. \tag{35}$$

Substituting this back into equation 29 with $\frac{dS}{dt} = 0$ provides the equation necessary to find S_{max}

$$\frac{\alpha V}{4\pi\gamma\rho_w} - GS_{max}\int_0^{S_{max}} \left(r^2(\tau) + 2G\int_\tau^{t_{max}} S(t)dt\right)^{1/2} n(S')dS' = 0. \tag{36}$$

Lamentably, an analytical solution for the integral in this equation is not possible. Different models vary in the way they attempt to solve the integral numerically, from simple empirical fits to elaborate population-splitting iterative procedures. Solving this integral is the crux of the parameterisation of cloud droplet formation.

4.3.1 Numerical models

While an analytical solution to equation 36 is not possible, there are various numerical aerosol activation models available which explicitly calculate the time-evolution of an aerosol distribution in terms of the growth of particles by condensation and coagulation [23, 11]. Most of these models do this within the framework of an adiabatically rising air parcel, but more detailed atmospheric conditions can be included in some models, such as incorporating the effects of entrainment of dry air into the parcel [11].

There are two reasons why such numerical models are not currently incorporated into GCMs. Firstly the coarse spatial grid of a GCM does not have the level of detail required by such models. Secondly, the computational expense of running a GCM at the time resolution required by such models is prohibitive. At least twenty time-steps are typically required between initial saturation and maximum supersaturation. Run at this resolution, the computation required by such detailed calculations would dominate the rest of the physics in most models [14].

One option for incorporating highly detailed models into GCMs is to run the numerical parcel model offline for a variety of different conditions and use a look-up table during the course of the atmospheric simulation. Unsurprisingly, this is only feasible when the activation process is only controlled by a few parameters. If the aerosol size distribution or composition are allowed to vary within the GCM, the size of look-up table required becomes impractical [14].

5 Parameterisation

In order to consolidate the complexities of the microphysical aerosol activation process with the relatively coarse temporal and spatial resolution of a GCM, the activation process must be parameterised in terms of the factors which influence it most significantly. Activation is a sub-grid scale process. This means it acts on a smaller spatial scale than the spatial grid of a GCM (typically $200 \times 200\,\mathrm{km}^2$ horizontally and with ~ 20 vertical levels in the troposphere) and the process occurs over a time scale far briefer than a typical timestep in a GCM (~ 20 minutes). Parameterising such processes means to express variability on smaller scales in terms of large-scale variables which are resolved in a GCM [32].

The parameterisation of activation must account for the competition between aerosol particles and for the dependence of the competition on particles size and distribution, and on the supersaturation forcing rate (i.e. updraught velocity). This approach relies on the parameterisation of other relevant sub-grid processes within the GCM, in particular updraught velocity. Some GCMs apply a gaussian distribution [9] or use turbulent kinetic energy as a proxy [31]. The parameterisation of sub-grid scale cloud dynamics must be improved in tandem with the parameterisation of aerosol activation for useful, reliable results to be obtained within a GCM.

Squires (1958) [44], Twomey (1959) [47], and Squires and Twomey (1960) [45] developed approximate expressions for the number of droplets which would form in a uniform, adiabatically rising air parcel. Squires assumed that all the CCN which become cloud droplets activate as soon as the supersaturation exceeds zero and grow from zero radius. Twomey simplistically assumes that when the critical supersaturation of a CCN is reached it will instantaneously grow from zero radius to its final radius. Both methods empirically relate the number of activated droplets to supersaturation as $N = cS^k$ (where c and k are empirically-derived constants), but not to any fundamental properties of the aerosols on which they form. Thus the number of droplets is not bound by the total aerosol number and systematic errors arise, particularly at high updraught velocities or low aerosol number. Incidentally, it has been shown [24, 20] that this form of the supersaturation spectrum is consistent with a power law aerosol size distribution. However, as discussed in section 3.1, there are serious limitations to the utility of such an approximation.

Ghan et al. (1993) [14] use a single log-normal size distribution to derive an activation parameterisation which is naturally bounded at high updraught velocity. Köhler theory is used to transform this number-size distribution to a number-supersaturation distribution and hence express the CCN spectrum $N(S)$, in terms of log-normal parameters. In contrast to the approach of Squires and Twomey, Ghan et al. neglect droplet growth beyond the point where the supersaturation exceeds the critical supersaturation of each CCN, i.e. beyond $S > S_c$. Instead, it is assumed that the radius of each particle when $S = S_{max}$ is given by the critical radius, r_c, of each particle. Clearly this is a severe over-simplification, since Köhler theory dictates that until $S = S_{max}$, particles with $S_c < S_{max}$ will grow spontaneously beyond r_c once $S = S_c$.

Abdul-Razzak et al. (1998) [4] combine the approaches of Twomey (1959) [47] and Ghan et al. (1993) [14] by using a log-normal aerosol size distribution and including droplet growth between the time of activation of each particle and the time when $S = S_{max}$. This is extended to a multimode version by Abdul-Razzak and Ghan (2000) [2]. For clarity, in section 5.1 the theory of the single mode case is outlined, although it is the multimode version which is tested in section 7, albeit only employing one of these modes. In 2002, Abdul-Razzak and Ghan extended the multimode log-normal parameterisation to the more general sectional representation of the aerosol size distribution, using many narrow log-normal modes [3].

5.1 Calculating S_{max} with the Abdul-Razzak and Ghan parameterisation

Abdul-Razzak and Ghan (1998, 2000) [4, 2] examine the integral in equation 35 in two limits. They define the parameter S_m as the supersaturation required to activate a particle with the count median radius, a_m. The size distribution is formulated in terms of the ratio $\frac{S_m}{S_{max}}$ where S_{max} is again the maximum supersaturation attained in the parcel, and hence a proxy for the radius of the smallest particle that activates, a_c by equation 22. For a log-normal size distribution, the CCN spectrum is represented as

$$n(S') = \frac{2N}{3S'\sqrt{2}\ln\sigma}\exp\left\{-\frac{\ln^2\left[\left(S_m/S'\right)^{2/3}\right]}{2\ln^2\sigma}\right\}. \tag{37}$$

In the first limit, the integral is considered for values of S_m small compared to S_{max} (i.e. where the radius of the smallest particle which activates, a_c is far less than the count median radius, a_m). In this case the growth term dominates the r^2 term in equation 36. Once the negligible r^2 term has been removed, the resulting integral is solved using Twomey's lower bound [47] to evaluate the inner integral. Substituting into equation 29 with $\frac{dS}{dt} = 0$ at S_{max} yields an expression for the upper bound of S_{max},

$$\frac{S_m}{S_{max}} = S_m\sqrt{J/\left(\eta + 3\xi\right)}, \tag{38}$$

where η and ξ are the dimensionless terms:

$$\eta = \frac{(\alpha V G)^{3/2}}{2\pi \rho_w \gamma N}; \quad \xi = \frac{2A}{3}\left(\frac{\alpha V}{G}\right)^{1/2} \tag{39}$$

and J is defined as

$$J \cong \operatorname{erfc}(u) - \frac{1}{2}\left(\frac{S_m}{S_{max}}\right)^2 \exp\left(\frac{3\ln\sigma}{\sqrt{2}}\right)^2 \operatorname{erfc}\left(u + \frac{3\ln\sigma}{\sqrt{2}}\right), \tag{40}$$

where

$$u \equiv \frac{\ln(a_c/a_m)}{\sqrt{2}\ln\sigma} = \frac{2\ln(S_m/S_{max})}{3\sqrt{2}\ln\sigma} \quad (\text{since} \quad \frac{a_c}{a_m} = \left(\frac{S_m}{S_{max}}\right)^{2/3}). \tag{41}$$

In the limit that S_m is comparable to S_{max} (and $a_m \sim a_c$), activated aerosols do not grow much beyond the point of activation. This is the limit proposed in Ghan et al. (1993) [14]. The growth term in the integral in equation 36 is negligible (as in the second limit in section 5.2.1). Integrating the CCN spectrum (equation 37) and substituting into equation 29 with $\frac{dS}{dt} = 0$ at S_{max} gives

$$\frac{S_m}{S_{max}} = U\frac{\xi}{\eta}, \tag{42}$$

where

$$U \equiv \exp\left(\frac{3\ln\sigma}{\sqrt{2}}\right)^2 \operatorname{erfc}\left(u - \frac{3\ln\sigma}{\sqrt{2}}\right). \tag{43}$$

Of course, this is really just a re-formulation of the problem rather than a solution to it. Both J and U are dependent on S_{max} and so an exact analytic solution is still impossible. Abdul-Razzak and Ghan propose an approximate solution based on numerical results of the full set of governing equations. These show that the ratio $(S_m/S_{max})^2$ is proportional to $(\xi/\eta)^{3/2}$ at small values of S_m and $\left(S_m^2/(\eta + 3\xi)\right)^{3/4}$ at large values of S_m. Over the full range of S_m the ratio is approximated by

$$\left(\frac{S_m}{S_{max}}\right)^2 = f_1(\ln\sigma)\left(\frac{\xi}{\eta}\right)^{3/2} + f_2(\ln\sigma)\left(\frac{S_m^2}{\eta + 3\xi}\right)^{3/4}, \tag{44}$$

where J and U are replaced by f_1 and f_2, functions of the standard deviation of the aerosol distribution. The authors use the following expressions for these functions[1], based again on numerical simulations with an error of less than 25% for a realistic range over all governing parameters [4]

$$f_1(\ln\sigma) = 0.5\exp\left(2.5(\ln\sigma)^2\right); \quad f_2(\ln\sigma) = 1 + 0.25\ln\sigma \tag{45}$$

Hence S_{max} is estimated from equation 44. The CCN spectrum is then integrated below this value to give the total number of droplets formed, from which the fraction of activated particles can be calculated.

---

[1] These are the functions used in the multi-mode version of the parameterisation, since this is the one which will be tested. They vary slightly from the single mode version numerically, reflecting a retuning of the parameterisation more appropriate for the accummulation mode particles that largely determine the total number activated [2].

5.2 Nenes & Seinfeld and Fountoukis & Nenes parameterisations

Building on the work of Abdul-Razzak and Ghan, in a quest for a more general parameterisation with less dependence on empirical information, Nenes and Seinfeld (2003) [35] developed a further cloud droplet activation parameterisation (hereafter NS). This allows for parameterisation of chemically complex aerosol with an arbitrary size distribution and mixing state (both internal and externally mixed aerosols can be included). Population splitting (outlined in section 5.2.2) allows for the explicit consideration of kinetic effects and as a result, the reliance on empirical information and correlations is substantially reduced, and eliminated altogether in a number of conditions [35].

The Fountoukis and Nenes (2005) [13] parameterisation (hereafter FN) improves further on NS by allowing for multimode log-normal aerosol size distributions (since these are prevalent in GCMs) and by including explicit size-dependence of water vapour diffusivity, which may be used to treat the film-forming ability of organic compounds [13]. Some aspects of these parameterisations are explored below.

5.2.1 Asymptotic limits in NS and FN model

Nenes and Seinfeld (2003) use a sophisticated bisection method to solve the integral in equation 35 by iteration. Following the notation in the paper (using diameter instead of radius), the integral alone is

$$I(0, S_{max}) = GS_{max} \int_0^{S_{max}} \left(D_p^2(\tau) + 2G \int_\tau^{t_{max}} S(t)dt \right)^{1/2} n(S')dS', \tag{46}$$

where $D_p(\tau)$ is the size of a CCN when it is exposed to the critical supersaturation, S_c, needed for it to activate, and τ is the amount of time taken to reach that critical supersaturation. Nenes and Seinfeld consider the two asymptotic limits of $I(0, S_{max})$ by comparing the two terms in the integral. In the first limit the CCN continue to grow significantly beyond the point where the ambient supersaturation equals their own critical supersaturation,

$$D_p^2(\tau) \ll 2G \int_\tau^{t_{max}} S(t)dt. \tag{47}$$

That is, the size at which the CCN activates, $D_p(\tau)$, is much less than the size it will finally grow to when $S = S_{max}$. In this case, Twomey's lower bound (1959) [47] can be used to approximate the supersaturation integral, as described in section 5:

$$\int_\tau^{t_{max}} S(t)dt \approx \frac{1}{2\alpha V} \left(S_{max}^2 - S(\tau)^2 \right), \tag{48}$$

where $S(\tau)$ is the parcel supersaturation at time τ. Subsituting back gives the integral in the first limit

$$I_1(0, S_{max}) = GS_{max} \int_0^{S_{max}} \left(\frac{1}{2\alpha V} \left(S_{max}^2 - S(\tau)^2 \right) \right)^{1/2} n(S')dS'. \tag{49}$$

The second limit occurs when the CCN do not grow significantly beyond the point where the ambient supersaturation exceeds their own critical supersaturation. (This is the limit employed by Ghan et al. (1993), in contrast to the choices of Squires and Twomey.)

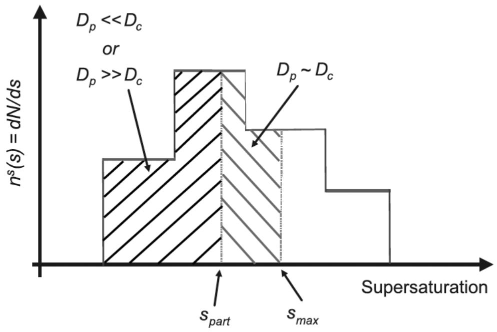

Fig. 7: Illustration in supersaturation space of the two subpopulations defined by the parameterisation, shown for the sectional representation used in NS. From Nenes and Seinfeld (2003) [35].

$$D_p^2(\tau) \gg 2G \int_{\tau}^{t_{max}} S(t)dt. \tag{50}$$

For the smallest CCN that activates, there is no time for growth beyond the critical size, $D_p(\tau)$ (or r_c). In this case the growth rate, $\frac{dr}{dt}$, is zero, so from equation 32,

$$S_c = \frac{A}{r_c} - B\left(\frac{r_s}{r_c}\right)^3. \tag{51}$$

Substituting for the expression for r_c (equation 23) yields[2]

$$r_c = \frac{2A}{3S_c}. \tag{52}$$

In the context of the NS and FN parameterisations, $D_p(\tau)$ is assumed to be equal to[3] $D_c = 2A/3S_c$ when the parcel supersaturation, S, equals the CCN critical supersaturation, S_c. This is a reasonable assumption when $\frac{dr}{dt} \ll \frac{dS}{dt}$ [9]. It assumes that a CCN is in equilibrium with the parcel supersaturation as it varies, and hence it reaches the critical radius simultaneously with the supersaturation reaching the CCN's critical supersaturation.

Substituting the approximation of equation 50 into equation 46 yields

$$I_2(S_c, S_{max}) = \frac{2}{3}AGS_{max} \int_{S_c}^{S_{max}} \frac{n(S')}{S_c} dS'. \tag{53}$$

5.2.2 Population Splitting

The two limits of integral 46 described above apply to CCN with contrasting attributes. The concept behind population splitting is that the aerosol distribution can be divided into two groups; CCN which are best described by the approximations made for equation 49 and CCN which are more appropriately described by the approximations underlying equation 53. In supersaturation

---

[2] Note that this is not an approximation, but an exact analytical expression [14].

[3] NS and FN define the Köhler A coefficient as twice the value defined in equation 15, which accounts for the factor of two between diameter and radius which appears to be missing here.

space, these two groups are divided by the partition supersaturation, S_{part}. The integral, $I(0, S_{max})$ (equation 46) is approximated by

$$I(0, S_{max}) = I_1(0, S_{part}) + I_2(S_{part}, S_{max}). \tag{54}$$

We assume there is only one S_{part} and that the upper bound of I_1 and the lower bound of I_2 coincide. Those CCN that would follow $I_1(0, S_{part})$ are those with either $D_p \ll D_c$ or $D_p \gg D_c$ and grow significantly beyond $S > S_c$. These CCN are on the left of S_{part} in figure 7. Those which do not grow significantly beyond $S = S_c$ are those with $D_p \approx D_c$ and follow $I_2(S_{part}, S_{max})$, (CCN between S_{part} and S_{max} in figure 7). The method for determining S_{part} is described in detail in Nenes and Seinfeld (2003) [35] and a brief outline follows.

The first choice for S_{part} is the CCN population critical supersaturation, such that $D_p^2(\tau) = 2G\int_{\tau}^{t_{max}} S(t)dt$. From equation 48 and substituting $D_p(\tau) = 2A/3S_{part}$, this eventually generates the quartic equation

$$f(S_{part}) = S_{part}^4 - S_{max}^2 S_{part}^4 + \frac{4A^2\alpha V}{9G} = 0. \tag{55}$$

There are two real roots to this equation if the discriminant, $\Delta = S_{max}^4 - \frac{16A^2\alpha V}{9G}$, is non-negative

$$\left(\frac{S_{part,1}}{S_{max}}\right)^2 = \frac{1}{2}\left[1 - \left(1 - \frac{16A^2\alpha V}{9S_{max}^4 G}\right)^{1/2}\right]; \quad \left(\frac{S_{part,2}}{S_{max}}\right)^2 = \frac{1}{2}\left[1 + \left(1 - \frac{16A^2\alpha V}{9S_{max}^4 G}\right)^{1/2}\right]. \tag{56}$$

These roots describe the behaviour of CCN that do not grow significantly beyond $S = S_c$, are those with $D_p \approx D_c$ and follow $I_2(S_{part}, S_{max})$. The second root is chosen in the model. When the discriminant is negative, equation 55 has no real roots. In this case S_{part} is calculated using a correlation derived from the regression of a large set of empirical S_{part} that reproduce the predictions of a detailed microphysics model:

$$\frac{S_{part}}{S_{max}} = min\left(0.666 \times 10^7 A S_{max}^{-0.3824}, 1.0\right). \tag{57}$$

Once S_{part} has been determined, equations 49 and 53 are substituted into equation 54, which approximates equation 46 and replaces the integral in equation 35. This can be solved for S_{max} using an iterative bisection method (see algorithm in figure 8). The final form of the parameterisation is

$$\frac{\pi}{2}\frac{\gamma\rho_w G S_{max}}{\alpha V}\left(\int_0^{S_{part}} D_p n^s(S')dS' + \int_{S_{part}}^{S_{max}} D_p n^s(S')dS'\right) - 1 = 0 \tag{58}$$

$$\frac{\pi}{2}\frac{\gamma\rho_w G S_{max}}{\alpha V}\left[I_1(0, S_{part}) + I_2(S_{part}, S_{max})\right] - 1 = 0. \tag{59}$$

The discriminant, Δ, expresses the extent of kinetic limitations throughout the droplet formation and depends on S_{max}, V and the timescale of water vapour diffusivity (embodied in G). $\Delta = 0$ marks the boundary between two growth regimes. For $\Delta > 0$, most CCN are free from kinetic limitations and S_{part} is determined without empirical information using the second root shown in equation 56. For $\Delta < 0$, kinetic limitations in droplet growth are strong throughout the entire population and S_{part} is calculated using the empirical relationship shown in equation 57, which is based on numerical simulations which were chosen so that $\Delta < 0$. This is the only part of the parameterisation which relies on empirical information, and it is only necessary for about 20% of cases [35, 13].

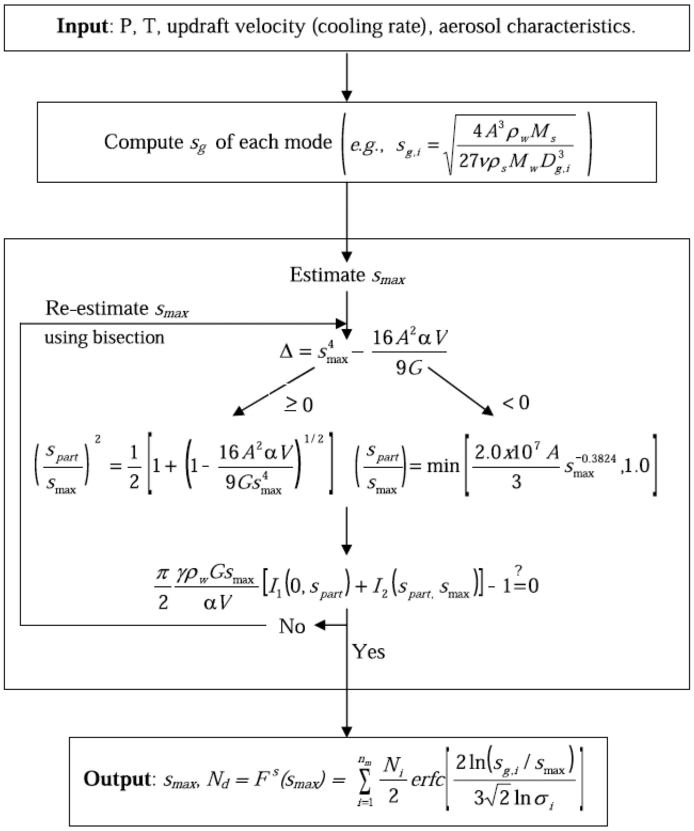

Fig. 8: Schematic representation of the parameterisation algorithm for the log-normal formulation (FN). From Fountoukis and Nenes (2005) [13].

6 Testing the Fountoukis and Nenes model

Source code for the FN cloud droplet formation parameterisation was provided by the authors, in Fortran 77. Some of the routines were updated to Fortran 90, although the bulk of the code was left untouched in Fortran 77.

Given atmospheric conditions (parcel temperature, pressure, updraught velocity) and a description of the aerosol distribution(s) including number of modes, aerosol number concentration, modal count median diameter, geometric standard deviation, density of soluble fraction, density of insoluble fraction, soluble mass fraction, molar mass of soluble fraction and Van't Hoff factor for soluble fraction, the model estimates S_{max}, the maximum supersaturation achieved in the parcel and hence calculates the number of cloud droplets which form. The fraction of activation, N_{act}, is defined as the ratio of the number concentration of initial aerosol particles, N_i, to final cloud droplets, N_d, and is often expressed as a percentage

$$N_{act} = 100\left(\frac{N_d}{N_i}\right). \tag{60}$$

As test cases, the authors provided three different sets of initial conditions and the expected output. Each case is described by three log-normal modes and so the multi-modal form of the model is required. The results were reproduced with no discrepancies, indicating that the code had ported

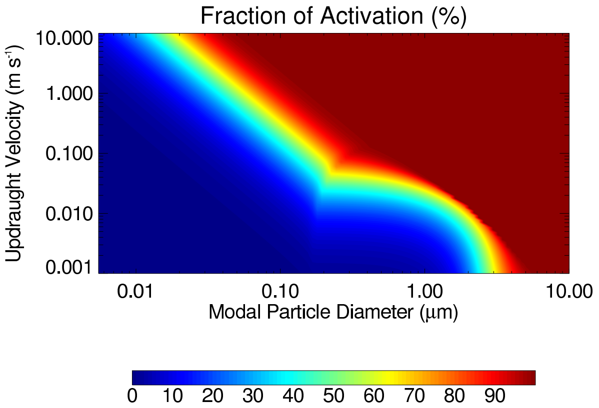

Fig. 9: Colour denotes fraction of activation, calculated using the FN model at each of one hundred incremental steps in log space over the given ranges of both updraught velocity and count median diameter (labelled here as modal particle diameter) for the Marine (North Atlantic) aerosol test case (see table 1).

successfully and worked as expected.

6.1 Diameter–velocity contour plots

For comparison with figures in Abdul-Razzak and Ghan (1998) [4], the FN model was used to examine how fraction of activation varies with dry particle modal count median diameter[4] and updraught velocity. Since the multi-modal model requires count median diameter to be specified for each mode, for simplicity only one mode (nucleation) was used, and count median diameter was varied from 0.005 to 10 μm for that one mode alone, encompassing the scope of all three modes in the test cases.

While critical radius increases with increasing dry radius, $r_c \propto r_s^{3/2}$ (equation 23), the critical supersaturation required for activation decreases as $S_c \propto r_s^{-3/2}$ (equation 22). Maximum supersaturation decreases slightly with increasing dry radius. Overall we expect these effects to combine such that fraction of activation, N_{act}, increases with modal count median diameter.

Figure 9 shows how the fraction of activation varies with increasing modal count median diameter for a fixed set of atmospheric conditions (temperature, $T = 298\,\mathrm{K}$, pressure, $p = 900\,\mathrm{mbar}$) aerosol composition and size distribution described in table 1. Since the updraught velocity of an air parcel has such an effect on the maximum achievable supersaturation (see equation 29), it was chosen as an appropriate atmospheric condition to vary at the same time, over the range 0.001 to 10 $\mathrm{m\,s^{-1}}$. Since both parameters extend over a range of orders of magnitude, incremental steps are spaced logarithmically to avoid over-sampling high values. Colour denotes fraction of activation.

At diameters less than 0.1 μm, the shape of the contour plot is as expected. At very low updraught velocities, for very small particles, there is no activation. As the size distribution is shifted along to higher values of median diameter and the updraught velocity is increased, the fraction of activated particles increases. However, between diameter 0.2 to 0.3 μm and updraught 0.03 to 0.1 $\mathrm{m\,s^{-1}}$ an abrupt discontinuity in the curves appears. From this point onwards the diagonal

---

[4] N.B. For a log-normal distribution, the median and the geometric mean are coincident [42]. In modelling, it is the median diameter which is commonly referrred to. In fact it is often described as the count (or number) median diameter to distinguish it from the mass median diameter. Diameter is frequently used instead of radius in aerosol science, although radius has been used here as much as possible for clarity and familiarity in equations [21].

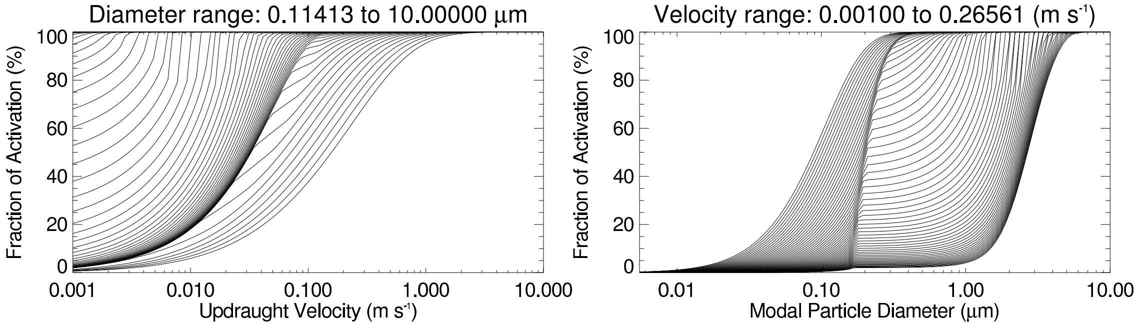

(a) (b)

Fig. 10: Marine (North Atlantic) aerosol test case. (a) vertical, and (b) horizontal slices through figure 9 over the region of the kink.

slope of the 50% contour line levels out such that between diameter 0.3 to 1.0 μm, increasing the diameter has little effect on the activated fraction, at fixed updraught velocity. Beyond 1.0 μm at updraught velocities below 0.03 $\mathrm{m\,s^{-1}}$ the diameter dominates, to such an extent that very low updraught velocities become almost insignificant. Above 0.03 $\mathrm{m\,s^{-1}}$and still beyond 1.0 μm, all particles activate.

Figures 10(a) and (b) show vertical and horizontal slices through the contour plot in figure 9, over the region of the kink. In figure 10(a) each line indicates the output from running the model at a fixed value of count median diameter, over the full range of updraught velocities used in the contour plot (figure 9). Moving from left to right across the plot, some of the first few lines (large diameter) are slightly kinked. The next few have almost vertical sections to them. Those with diameters over the region of the kink have definite angles in otherwise smooth curves. The last few lines (smaller diameter) are smooth sigmoid curves. In figure 10(b), each line shows the output from running the model at fixed updraught velocity, over the full range of count median diameter. The first sigmoid curves on the left (high updraught velocity) soon give way to many lines with an abrupt kink in them. The smooth sigmoid curves expected in fact have discontinuities in both diameter and updraught velocity.

6.1.1 The 'bug fix'

The authors of the model provided a bug fix to the original code, a factor of two in one of the manifestations of the Köhler A coefficient (section 2.2.1) used in the calculation of S_{max}. The same figures are repeated with the code including the bug fix. In figure 11, the kink in the contour plot is more abrupt than without the bug-fix. This is further elucidated by looking at the vertical and horizontal slices through this plot in figures 12(a) and (b). It is clear that the discontinuities have become even more pronounced by the introduction of the bug fix. Indeed the lines are no longer even monotonically increasing functions.

6.1.2 Increasing resolution of the contour plot

In order to generate the contour plot in figure 9, the model is run over a matrix of one hundred values of updraught velocity by one hundred values of count median diameter, logarithmically spaced (10,000 times in all). To check that the kink is not a result of some error generated at any of these particular values, the same plot is reproduced with a finer resolution, using 1000 steps over diameter

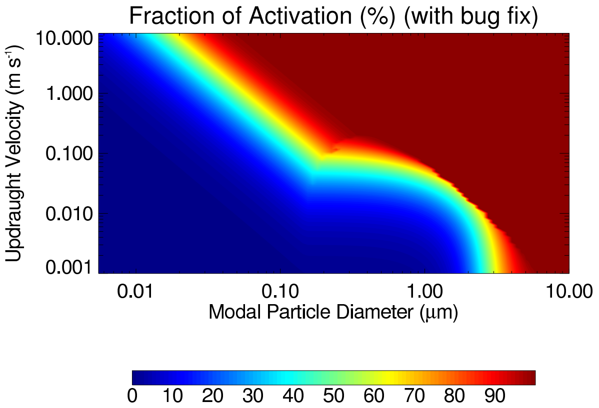

Fig. 11: As figure 9 (marine (North Atlantic) aerosol test case) with bug fix.

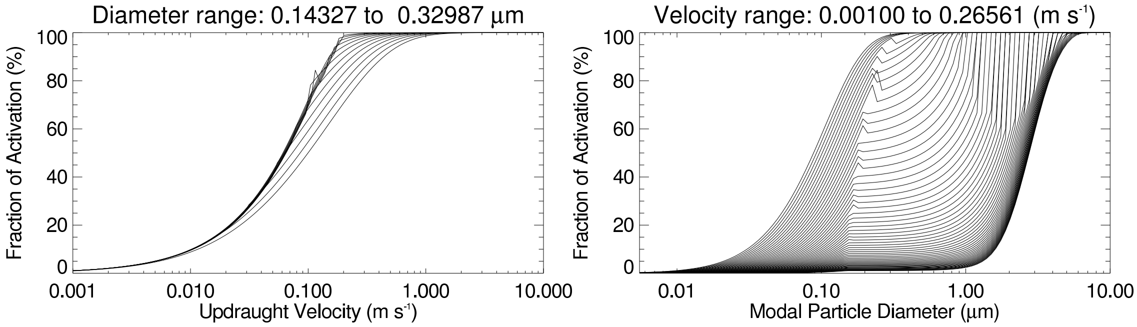

(a) vertical slices

(b) horizontal slices

Fig. 12: Marine (North Atlantic) aerosol test case with bug fix. (a) vertical, and (b) horizontal slices through figure 11 over the region of the kink.

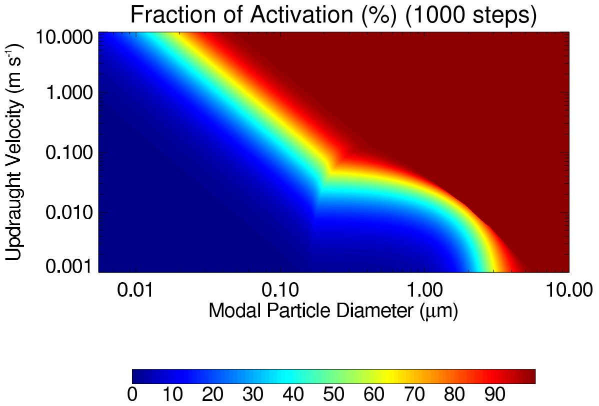

Fig. 13: Colour denotes fraction of activation, calculated at each of one thousand incremental steps in log space over the given ranges of both updraught velocity and count median diameter, for the marine (North Atlantic) aerosol test case, as in figure 9.

and updraught velocity rather than 100. The result is shown in figure 13, and the kink does not disappear.

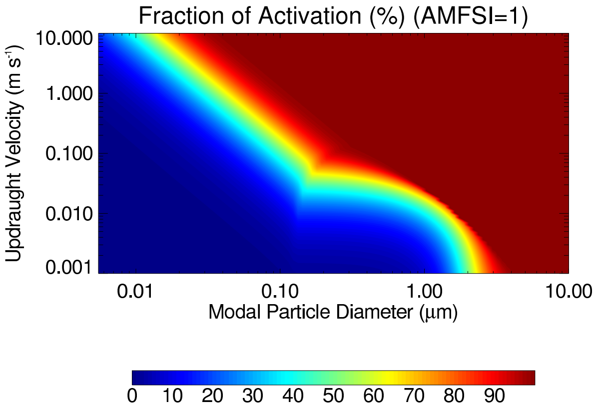

Fig. 14: Marine (North Atlantic) aerosol test case with enitrely soluble aerosol, (soluble mass fraction increased to 1.0 from 0.33).

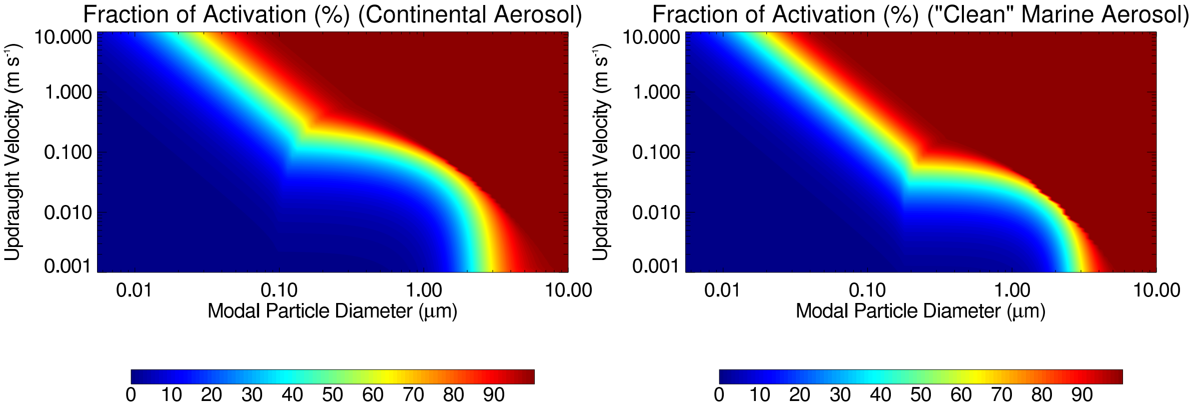

(a) (b)

Fig. 15: Colour denotes fraction of activation for (a) continental aerosol test case and (b) “clean” marine aerosol test case, defined in table 1.

6.1.3 Changing soluble mass fraction

Figure 14 shows the result of setting the soluble mass fraction of the aerosol distribution to 1.0 (entirely soluble), which is that the fraction of activation saturates at slightly smaller diameters. In the marine (North Atlantic) aerosol test case this value is originally 0.33 (in figure 9, see table 1). As expected, when the input aerosol is entirely insoluble, there is no activation at all (no figure shown).

6.1.4 Varying input parameters

To verify that the kink is not simply a problem with the marine (North Atlantic) aerosol test case, figures 15(a) and (b) show the same contour plot with different input test cases: a continental aerosol distribution and a “clean” marine aerosol distribution, outlined in table 1. Ambient temperature and pressure are the same as the North Atlantic case ($T = 298\,\mathrm{K}$, $p = 900\,\mathrm{mbar}$). While the position of the curve on the plot changes depending on test case, the unexpected shape of the surface is present for all three test cases.

	Marine (North Atlantic)	Continental	“Clean” marine (South Oceans)
CCN number conc. (m^{-3})	230×10^6	1000×10^6	310×10^6
Geometric standard deviation	1.47	1.6	1.4
Soluble mass fraction	0.33	0.5	0.33

Tab. 1: Input parameters for test cases, provided by A. Nenes

Updraught velocity ($m\,s^{-1}$)	5.0
Temperature (K)	283.0
Pressure (Pa)	8×10^4
CCN number conc. (m^{-3})	200×10^6
Count median radius (μm)	0.01
Geometric standard deviation	2.5

Tab. 2: Soluble $(NH_4)_2\,SO_4$

7 Abdul-Razzak and Ghan model testing

The Abdul-Razzak and Ghan aerosol activation scheme (ARG) was implemented by Philip Stier in a preliminary version of the aerosol–climate model, ECHAM5-HAM [46], with explicit aerosol–cloud coupling [33]. This code was extracted from ECHAM and adapted from a three dimensional GCM scheme to a zero dimensional box model with no spatial dependence (effectively a single grid point). Given the appropriate input parameters, the box model simply calculates the number density of droplets which would form at a single point in space. The scheme used is the multimode aerosol activation scheme (2000) which is an extension of the 1998 single log-normal mode scheme. The multimode version caters for the case of multiple externally mixed log-normal modes, each with a uniform internal mixture of soluble and insoluble material (i.e. each mode is of a uniform (internally mixed) composition, and multiple modes may be externally mixed together). In the tests which follow, only one mode was used, for comparison with the tests of the FN model (section 6.1).

In order for the box model to work independently of the GCM, a number of subroutines were written to calculate input parameters which would have come straight from the GCM, such as specific humidity, dry air density, mass mixing ratio of aerosols and saturated vapour pressure of water. Where the same parameters exist in both models these routines were written to emulate the input conditions to the FN model.

7.1 Test case: soluble ammonium sulphate

Abdul-Razzak and Ghan (1998) [4] (single log-normal mode scheme) display various plots showing a comparison between the parameterisation and a numerical model, using a test case of soluble $(NH_4)_2\,SO_4$. Three of these figures were replicated using only one mode of the multimode box model, ARG, described above, with the input conditions shown in table 2.

Figure 16 shows fraction of activation as a function of count median radius. While the shape of the curve is similar to that published, the curve in figure 16(a) is much steeper than the one in the paper (b). At a count median radius of 0.01μm, figure 16(b) shows a fraction of activation of about 50% compared to over 80% in figure 16(a). The curve in (a) saturates at 100% before 0.1μm, while the curve in figure (b) does not reach 100% activation over the range shown.

In figure 17, fraction of activation is shown as a function of initial aerosol number concentration,

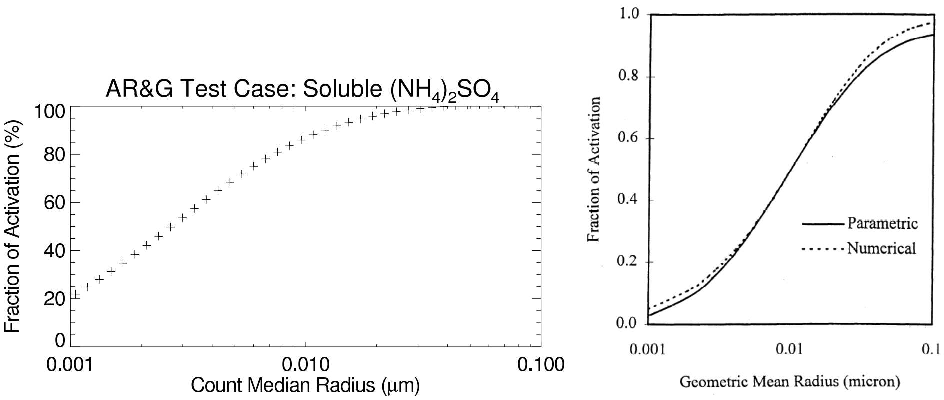

(a) (b)

Fig. 16: Fraction of activation as a function of count median radius shown (a) for our implementation of ARG and (b) as published [4].

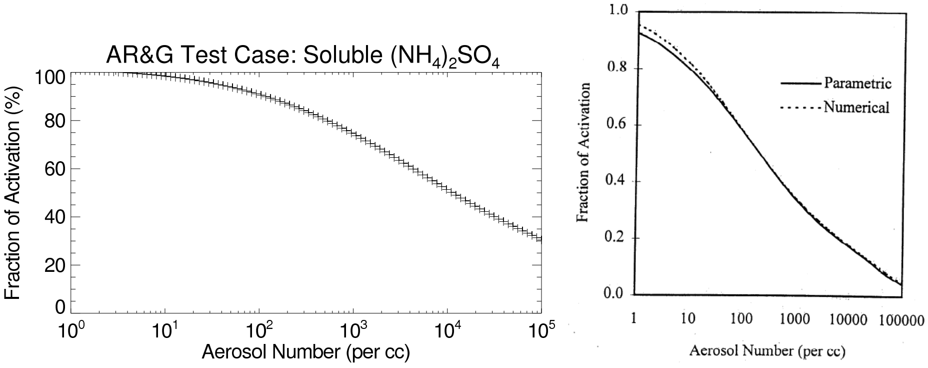

(a) (b)

Fig. 17: Fraction of activation as a function of initial aerosol number concentration shown (a) for our implementation of ARG and (b) as published [4].

N. The expected decreasing trend is demonstrated in both (a) and (b) At high values of N, depletion of water vapour by the sheer quantity of activated droplets is a strongly limiting factor in how many particles can activate [8]. However, while in (b) $N_{act} \approx 5\%$ when $N = 10,000\,\mathrm{cm}^{-3}$, in (a) $N_{act} \approx 30\%$. At very low values of N, (a) is saturated at 100% activation, which would seem reasonable given the initial conditions of the test case. This is not seen in (b), from the paper, where N_{act} does not quite saturate. Maximum supersaturation, S_{max} was also plotted as a function of N, shown in figure 18. The maximum supersaturation achievable in the parcel decreases strongly with increasing aerosol number concentration, as the available water vapour is depleted by ever more activating particles.

Fraction of activation as a function of the spread of the log-normal distribution is shown in figures 19(a) and (b). N_{act} is plotted against $\ln\sigma$, where σ is the geometric standard deviation of the mode. As $\ln\sigma$ increases, the distribution broadens. More particles have a dry radius further from the median, and a critical supersaturation further from S_{max} and hence the fraction of activation decreases. While both figures show this trend, the shapes of the curves differ substantially. In (a), $N_{act} = 100\%$ at low values of $\ln\sigma$, whereas in (b) the curve drops steeply away from high N_{act},

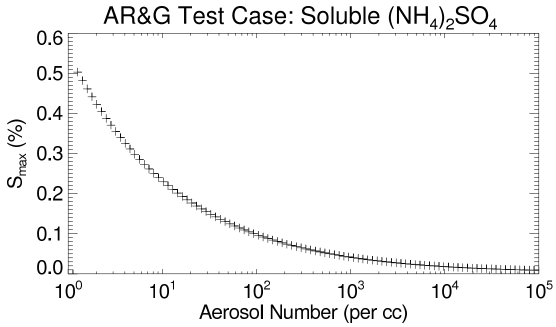

Fig. 18: Maxiumum achieved supersaturation as a function of initial aerosol number concentration shown for our implementation of ARG.

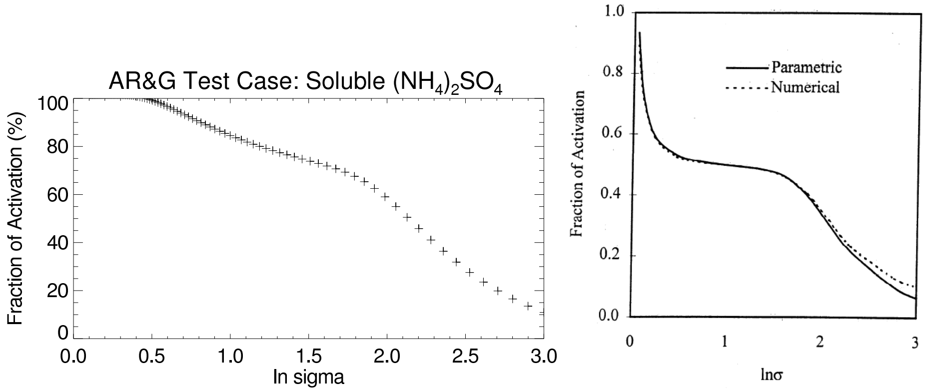

(a) (b)

Fig. 19: Fraction of activation as a function of geometric standard deviation of the mode shown (a) for our implementation of ARG and (b) as published [4].

levelling out at about 50%. At high values of $\ln\sigma$ the two figures are similar.

The reason for the discrepancies between the figures from the paper and those from our implementation in a box model is currently under active investigation.

7.1.1 Diameter–velocity contour plot

For comparison with the contour plots of fraction of activation in the FN tests, figures 9 and 15, the ARG model was run over the same range of updraught velocity and count median diameter for the soluble ammonium sulphate test case. Fraction of activation is again shown as a function of these two variables in figure 20. The shape of the surface makes much more physical sense than figure 9. Up to a count median diameter of 0.1μm, N_{act} increases with increasing updraught velocity and increasing count median diameter. Beyond 0.1μm, the particles are already such a size that increasing the median value of the distribution no longer has a noticeable effect on the fraction of activation, and the effect of varying updraught velocity dominates.

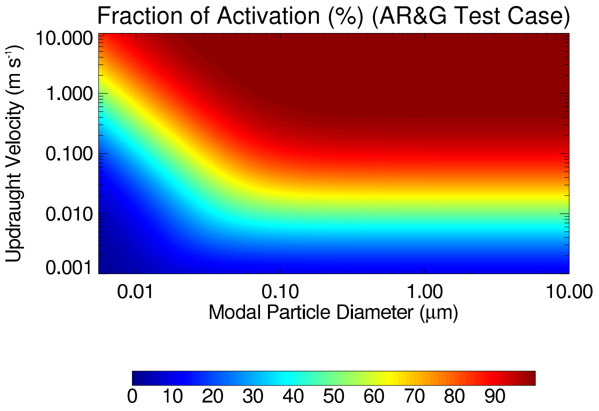

Fig. 20: Colour denotes fraction of activation, calculated at each of one hundred incremental steps in log space over the given ranges of both updraught velocity and count median diameter (labelled here as modal particle diameter) for the soluble $(NH_4)_2\,SO_4$ test case (see table 2).

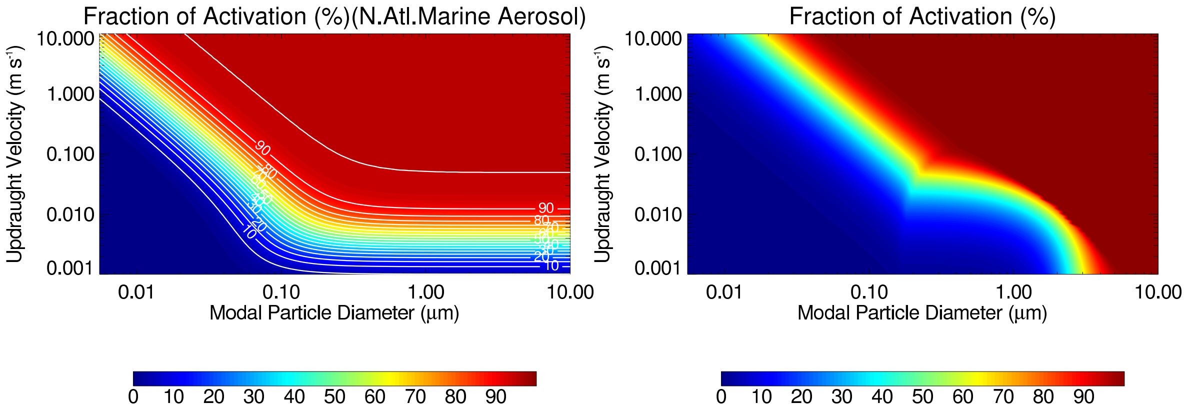

(a)

(b)

Fig. 21: Marine (North Atlantic) aerosol test case calculated with (a) ARG model and (b) FN model.

8 Model intercomparison

There is a striking contrast between the two models, as shown in the diameter–velocity contour plots in figures 9 and 20. Clearly, for a fair comparison, the same input conditions must be used for each model. The ARG model was altered to be able to accept the same format of input conditions as the FN model. Rigorous testing was undertaken to ensure the same values of every input parameter were used in both models. This included testing the results of all initial calculations performed by both models, such as the calculation of the Köhler A and B coefficients (equations 15 and 19).

However, despite such checks, serious discrepancies were still found between the two models, in each of the three test cases. Figures 21, 22 and 23 show contour plots of fraction of activation for each of the three test cases provided, for both models. Table 1 outlines the differences in input parameters between the three different cases. Atmospheric conditions ($T = 298\,\mathrm{K}$, $p = 900\,\mathrm{mbar}$) and all other variables were held constant between the different examples.

In an attempt to locate the cause of the problem in the Nenes model, further methodical checks

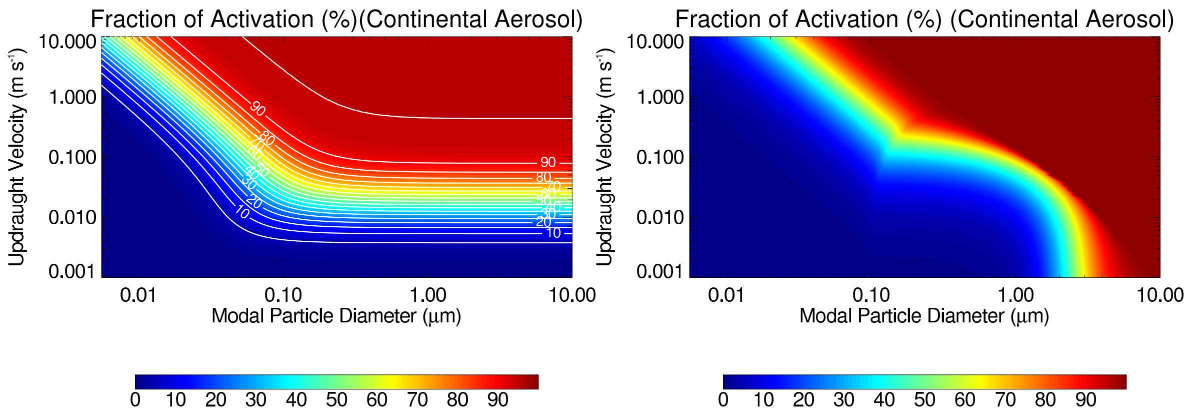

(a) (b)

Fig. 22: Continental aerosol test case calculated with (a) ARG model and (b) FN model.

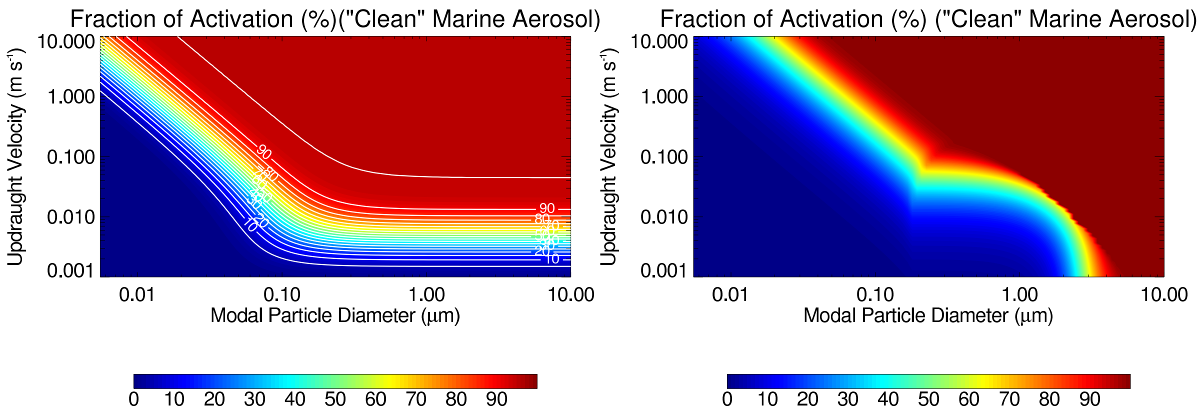

(a) (b)

Fig. 23: "Clean" marine aerosol test case calculated with (a) ARG model and (b) FN model.

were undertaken. The code for both models was checked against the respective papers, and the papers were checked against one another and the physics described above to ensure the equivalence of the different formulations of the equations preceding and following the calculation of S_{max} (where the models diverge).

Many of the figures included so far show fraction of activation as a function of other variables. However, N_{act} is not a direct equivalent of S_{max}. Once S_{max} is known, the CCN spectrum must be integrated to give the number concentration of droplets which form, which is then used to calculate N_{act}. Before going any further, the integration routines of both models were checked to ensure an error was not being introduced at this stage. Using the soluble ammonium sulphate test case (table 2), both models were run over a range of fixed values of S_{max}, in order to test their integration routines.

Figures 24(a) and (b) show N_{act} as a function of prescribed S_{max} at a fixed point in diameter–velocity parameter space (see table 2 again). Both models exhibit a smooth relation between N_{act} and S_{max} indicating no problem in the conversion between them using the integration routine, albeit only at the specified updraught and median diameter. As an additional check, the vertical line on

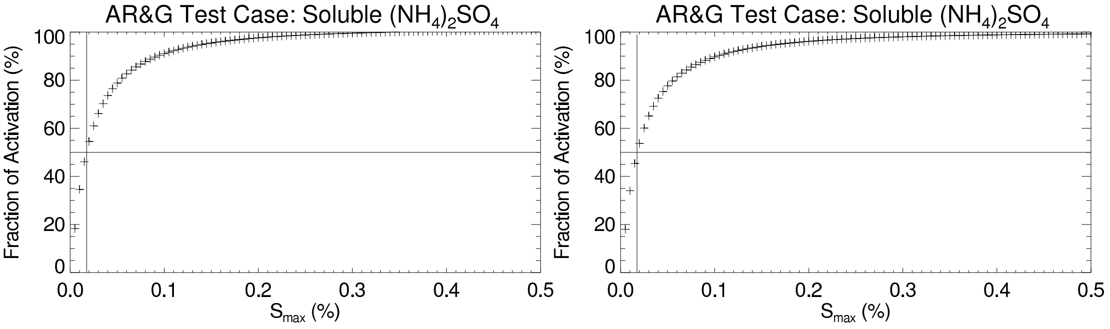

(a) ARG Model (b) FN Model

Fig. 24: N_{act} as a function of prescribed S_{max} for (a) ARG model and (b) FN model, both using the soluble $(\mathrm{NH_4})_2\,\mathrm{SO_4}$ test case (table 2).

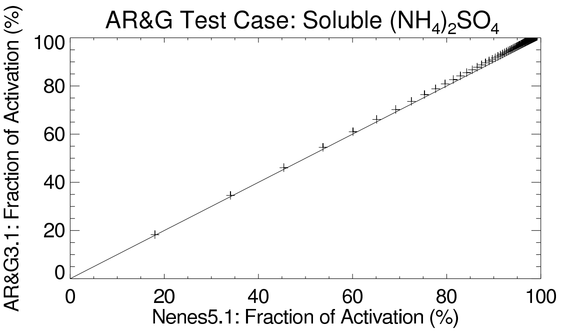

(a)

Fig. 25: Comparison of N_{act} calculated by ARG and FN models, over S_{max} range: 0.005% to 0.5%

each graph indicates the position of S_m, the supersaturation required to activate particles with the count median radius. In both figures (a) and (b), the position of S_m intersects the curve at $N_{act} = 50\%$, as expected at the count median. Figure 25 shows the a scatter plot between the two models in their calculation of N_{act} over the prescribed S_{max} range: 0.005% to 0.5%. The solid line shows a 1:1 relationship. The figure shows that the ARG model slightly exceeds the FN model at high S_{max}, but the difference is not the cause of the massive discrepancies between the contour plots. The integration routines in both models were judged to be fairly robust.

As a final further check that the problem is in the calculation of S_{max} in the FN model, rather than later in the algorithm (i.e. the step between S_{max} and N_{act}), the contour plots are repeated in figure 26, with S_{max} rather than N_{act} plotted as a function of updraught velocity and count median diameter. Figure 26(a) shows the plot for the ARG model, with the marine (North Atlantic) input conditions. The smooth surface across the broad but typical range of diameter and velocity seems reasonable. Figure 26(b) shows the same plot with the same input conditions for the FN model. The colour scale is the same for both figures. There is clearly a problem with the calculation of S_{max} in the FN model, over this range of updraught velocity and count median diameter. Unfortunately, this is a physically reasonable range for aerosol activation [42] and this problem must be resolved before the FN model can be implemented in the Met Office GCM.

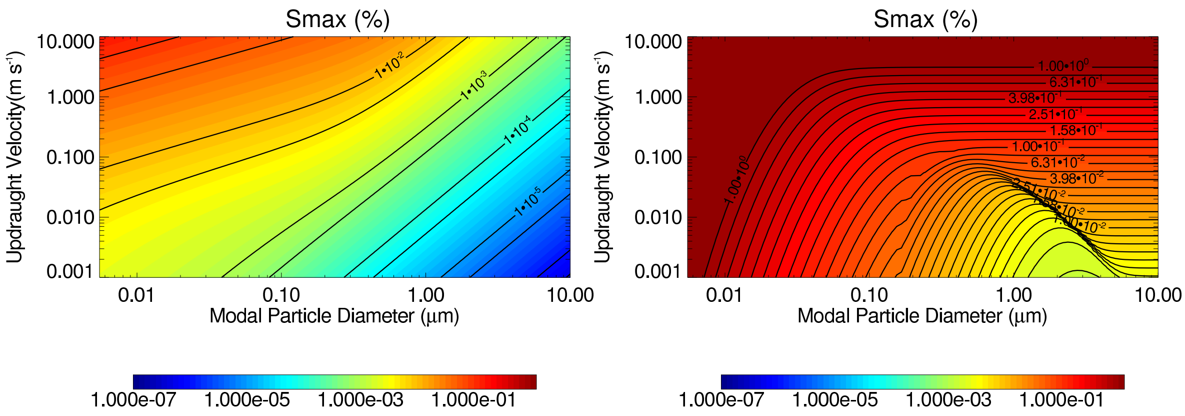

(a) (b)

Fig. 26: Maximum achievable supersaturation as a function of count median diameter, for the marine (North Atlantic) aerosol test case. A log colour scale highlights the range of orders of magnitude of S_{max} over this range of updraught and diameter. The same colour scale is used for (a) ARG model and (b) FN model.

9 Future Plans

Michaelmas 2008

The immediate priority for the advancement of this project is to implement one of these cloud droplet formation parameterisations into the Hadley Centre GCM, HadGEM2. As shown, the FN parameterisation has less reliance on empirical information, and has been developed to incorporate more detailed aspects of droplet formation, such as the explicit size-dependence of water vapour diffusivity, which may be used to treat the film-forming ability of organic compounds [13]. Nevertheless, the above tests indicate that the ARG parameterisation currently provides more reliable results. We are in correspondence with one of the authors of FN, Athanasios Nenes, and an investigation into the problem in the calculation of S_{max} is underway.

There are still several tests which I intend to perform on the FN parameterisations:

- Re-run the tests of FN using one of the other modes defined in the test cases provided by the author. It has been pointed out that so far only the nucleation mode has been tested (albeit over a diameter range encompassing all three modes).
- It has been speculated that the problem in the calculation of S_{max} occurs in the region of S_{part}, where the asymptotic limits are merged. This requires further investigation.

Once this has been resolved, either the FN or ARG parameterisation will be extended to three dimensional model and implemented in the GCM. This will involve at least a fortnight at the Met Office.

- I am also interested in two issues related to modelling droplet formation, the sub-grid parameterisation of updraught velocity and the effect of existing cloud droplets on the activation of further aerosols and hope to pursue these interests.

- In October I am planning to attend the 7th AeroCOM workshop (Aerosol Comparisons between Observations and Models). Discussions here will help inform plans for my own comparisons of aerosol–cloud interactions in the HadGEM2 and satellite observations from the A-train.

Hilary 2009

Since "fraction of activation" is not currently a property retrievable by satellite remote sensing instruments, output from the GCM will need to be formulated in terms of quantities which are observable, such as cloud droplet effective radius and aerosol optical depth. Quantities relating to simulated cloud and aerosol fields from the model can then be compared with satellite data through correlation studies. Spurious correlations will then be investigated.

Trinity 2009

Results of correlation studies and model/satellite comparisons will be used to iteratively improve the model. The model could be used to test consistency of satellite data.

Michaelmas 2009

Eventually, the refined model will be used for quantification of radiative forcing of the indirect aerosol effect, and aerosol–cloud–climate feedback studies.

Hilary & Trinity 2010

Writing up and completion of thesis.

10 Transferable skills

Transferable skills I have developed this year (as categorised in the Research Councils' Skills List):
A 1,2,3,4,5,6.
B 4.
C 1,2,3,4.
D 1,2,3,4,5,6,7.
E 1,2.
F 1,2,3.
G 3,4.

References

[1] J. P. D. Abbatt, K. Broekhuizen, and P. P. Kumal. Cloud condensation nucleus activity on internally mixed ammonium sulfate/organic acid aerosol particles. *Atmospheric Environment*, 39(26):4767–4778, 2005.

[2] H. Abdul-Razzak and S. J. Ghan. A parameterization of aerosol activation 2. multiple aerosol types. *Journal of Geophysical Research*, 105(D5):6837–6844, 2000.

[3] H. Abdul-Razzak and S. J. Ghan. A parameterization of aerosol activation 3. sectional representation. *Journal of Geophysical Research*, 107(D3):4026, 2002.

[4] H. Abdul-Razzak, S. J. Ghan, and Rivera-Carpio C. A parameterization of aerosol activation 1. single aerosol type. *Journal of Geophysical Research*, 103(D6):6123–6131, 1998.

[5] J. Aitchison and J. A. C. Brown. *The Lognormal Distribution Function.* Cambridge University Press, Cambridge, UK, 1957.

[6] B. A. Albrecht. Aerosols, cloud microphysics, and fractional cloudiness. *Science*, 245(4923):1227–1230, 1989.

[7] M.O. Andreae and D. Rosenfeld. Aerosol–cloud–precipitation interactions. part 1. the nature and sources of cloud-active aerosols. *Earth-Science Reviews*, 89(1-2):13–41, July 2008.

[8] O. Boucher and U. Lohmann. The sulfate-CCN-cloud albedo effect - a sensitivity study with two general-circulation models. *Tellus B Series*, 47:281–300, 1995.

[9] C. C. Chuang, J. E. Penner, K. E. Taylor, A. S. Grossman, and J. J. Walton. An assessment of the radiative effects of anthropogenic sulphate. *Journal of Geophysical Research*, 102:3761–3778, 1997.

[10] W. E. Clark and K. T. Whitby. Concentration and size distribution measurement of atmospheric aerosols and a test of the theory of self-preserving size distributions. *Journal of the Atmospheric Sciences*, 24:677–687, 1967.

[11] A. Flossman, W. Hall, and H. R. Pruppacher. A theoretical study of the wet removal of atmospheric pollutants: part i: The redistribution of aerosol particles captured through nucleation and impaction scavenging by growing cloud drops. *Journal of the Atmospheric Sciences*, 42:583–606, 1985.

[12] P. Forster, V. Ramaswamy, P. Artaxo, T. Berntsen, R. Betts, D. W. Fahey, J. Haywood, J. Lean, D. C. Lowe, G. Myhre, J. Nganga, R. Prinn, G. Raga, M. Schulz, and R. Van Dorland. *Climate Change 2007: The Scientific Basis. Contribution of working group I to the Fourth Assessment Report of the Intergovernmental Panel on Climate Change.* Cambridge University Press, Cambridge, UK, 2007.

[13] C. Fountoukis and A. Nenes. Continued development of a cloud droplet formation parameterization for global climate models. *Journal of Geophysical Research*, 110(D11212), 2005.

[14] S. J. Ghan, C. C. Chuang, and J. E. Penner. A parameterization of cloud droplet nucleation 1. single aerosol type. *Atmospheric Research*, 30(4):198–221, December 1993.

[15] J. A. Goff and S. Gratch. Low-pressure properties of water from -160 to 212 °F. *Transactions of the American Society of Heating and Ventilating Engineers*, (95-122), 1946.

[16] I. Gultepe and G. Isaac. The relationship between cloud droplet and aerosol number concentrations for climate models. *International Journal of Climatology*, 16:941–946, 1996.

[17] K. E. H. et al. Hartz. Cloud condensation nuclei activation of limited solubility organic aerosol. *Atmospheric Environment*, 40(4):605–617, 2006.

[18] T. Hatch and S. P. Choate. Statistical description of the size properties of non-uniform particulate substances. *Journal of the Franklin Institute*, 207:369, 1929.

[19] D. A. Hegg. Impact of gas phase HNO_3 and NH_3 on microphysical processes in atmospheric clouds. *Geophysical Research Letters*, 27(15):2201–2204, 2000.

[20] F. Herbert. CCN-equilibrium theory. *Meteorol. Rundsch*, 65:82–87, 1986.

[21] W. C. Hinds. *Aerosol technology: properties, behavior, and measurement of airborne particles.* Wiley, New York; Chichester, 2nd edition, 1999.

[22] T. Hussein. Indoor and outdoor aerosol particle size characterization in Helsinki. Report Series in Aerosol Science 74, University of Helsinki, 2005.

[23] J. Jensen and R. J. Charlson. On the efficiency of nucleation scavenging. *Tellus B Series*, 36:367–375, 1984.

[24] J. E. Jiusto and G. G. Lala. CCN-supersaturation spectra slopes (k). *J. Reich. Atmos*, 15:303–311, 1981.

[25] A. Jones, D. L. Roberts, and A. Slingo. A climate model study of indirect radiative forcing by anthropogenic sulphate aerosols. *Nature*, 370:450–453, 1994.

[26] C. E. Junge. Die rolle der aerosole und der gasformingen der luft im spurenstoffhaushalt der troposphere. *Tellus*, 5:1–26, 1953.

[27] M et al. Kanakidou. Organic aerosol and global modelling: a review. *Atmospheric Chemistry and Physics*, 5:1053–1123, 2005.

[28] J. T. Kiehl, T. L. Schneider, and P. J. Rasch. Radiative forcing due to sulfate aerosols from simulations with the national center for atmospheric research community climate model, version 3. *Journal of Geophysical Research*, 105(D1):1441–1457, 2000.

[29] H. Köhler. The nucleus in and the growth of hygroscopic droplets and the growth of hygroscopic droplets. *Transactions of the Faraday Society*, 32:1152–1161, 1936.

[30] M. et al. Kulmala. The effect of atmospheric nitric acid vapor on cloud condensation nucleus activation. *Journal of Geophysical Research*, 98(D12):22,949–22,958, 1993.

[31] U. Lohmann, J. Feichter, C. C. Chuang, and J. E. Penner. Predicting the number of cloud droplets in the ECHAM GCM. *Journal of Geophysical Research*, 104:9169–9198, 1999.

[32] U. Lohmann, J. Quaas, S. Kinne, and J. Feichter. Different approaches for constraining global climate models of the anthropogenic indirect aerosol effect. *Bulletin of the American Meteorological Society*, pages 243–249, February 2007.

[33] U. Lohmann, P. Stier, C. Hoose, S. Ferrachat, S. Kloster, E. Roeckner, and J. Zhang. Cloud microphysics and aerosol indirect effects in the global climate model echam5-ham. *Atmospheric Chemistry and Physics*, 7(13):3425–3446, 2007.

[34] G. McFiggans, P. Artaxo, U. Baltensperger, H. Coe, M. C. Facchini, G. Feingold, S. Fuzzi, M. Gysel, A. Laaksonen, U. Lohmann, T. F. Mentel, D. M. Murphy, C. D. O'Dowd, J. R. Snider, and E. Weingartner. The effect of physical and chemical aerosol properties on warm cloud droplet activation. *Atmospheric Chemistry and Physics*, 6(9):2593–2649, 2006.

[35] A. Nenes and J. H. Seinfeld. Parameterization of cloud droplet formation in global climate models. *Journal of Geophysical Research*, 108(D14):4415, 2003.

[36] A. et al. Nenes. Can chemical effects on cloud droplet number rival the first indirect effect? *Geophysical Research Letters*, 29(17):1848, 2002.

[37] H. R. Pruppacher and J. D. Klett. *Microphysics of Clouds and Precipitation.* Reidel, Dordrecht, 1997.

[38] J. P. et al. Putaud. European aerosol phenomenology–2: chemical characteristics of particulate matter at kerbside, urban, and background sites in Europe. *Atmospheric Environment*, 38(16):2579–2595, 2004.

[39] J. Quaas, O. Boucher, and U. Lohmann. Constraining the total aerosol indirect effect in the LMDZ and ECHAM4 GCMs using MODIS satellite data. *Atmospheric Chemistry and Physics*, 6(4):947–955, 2006.

[40] V. Ramaswamy, O. Boucher, J. Haigh, D. Hauglustaine, J. Haywood, G. Myhre, T. Nakajima, G. Y. Shi, and S. Solomon. *Climate Change 2001: The Scientific Basis. Contribution of working group I to the Third Assessment Report of the Intergovernmental Panel on Climate Change.* Cambridge University Press, Cambridge, UK, 2001.

[41] R. R. Rogers and M. K. Yau. *A Short Course in Cloud Physics.* Pergamon Press, Oxford, UK, 1989.

[42] J. H. Seinfeld and S. N. Pandis. *Atmospheric Chemistry and Physics: from Air Pollution to Climate Change.* John Wiley, New York, 1998.

[43] M. L. Shulman, M. C. Jacobson, R. J. Charlson, R. E. Synovec, and T. E. Young. Dissolution behaviour and surface tension effects of organic compounds in nucleating cloud droplets. *Geophysical Research Letters*, 23:277–280, 1996.

[44] P. Squires. The microstructure and colloidal stability of warm clouds, ii, the causes of the variations in microstructure. *Tellus*, 10:262–271, 1958.

[45] P. Squires and S. Twomey. *Physics of Precipitation*, volume 5 of *Geophys. Monogr. Ser.*, chapter The relation between cloud droplet spectra and the spectrum of cloud nuclei. AGU, Washington, D. C., 1960.

[46] P. Stier, J. Feichter, S. Kinne, S. Kloster, E. Vignati, J. Wilson, L. Ganzeveld, I. Tegen, M. Werner, Y. Balkanski, M. Schulz, O. Boucher, A. Minikin, and A. Petzold. The aerosol-climate model ECHAM5-HAM. *Atmospheric Chemistry and Physics*, 5(4):1125–1156, 2005.

[47] S. Twomey. The nuclei of natural cloud formation, part ii: The supersaturation in natural clouds and the variation of cloud droplet concentration. *Geofisica Pura e Applicata*, 43:243–249, 1959.

[48] S. Twomey. Pollution and planetary albedo. *Atmospheric Environment*, 8:1251–1256, 1974.

[49] K. Von der Emde and U. Wacker. Comments on the relationship between aerosol spectra, equilibrium drop size spectra, and CCN spectra. *Beitr. Phys. Atmos.*, 66:157–162, 1993.

[50] J. M. Wallace and P. V. Hobbs. *Atmospheric Science: An Introductory Survey.* Academic Press, 2nd edition, 2006.

[51] J. Warner. A reduction of rain associated with smoke from sugarcane fires-an inadvertent weather modification. *Journal of Applied Meteorology*, 7:247–251, 1968.

[52] K. T. Whitby. The physical characteristics of sulfur aerosols. *Atmospheric Environment*, 12:135–159, 1978.